



Investigation on Mechanical Properties, AE Characteristics, and Failure Modes of Longmaxi Formation Shale in Changning, Sichuan Basin, China

Chengxing Zhao^{1,2} · Jianfeng Liu^{1,2,3} · Deng Xu^{1,2} · Liangquan Zhang^{1,2} · Cheng Lyu^{1,2} · Yi Ren^{1,2}

Received: 11 June 2022 / Accepted: 25 October 2022 / Published online: 9 November 2022
© The Author(s), under exclusive licence to Springer-Verlag GmbH Austria, part of Springer Nature 2022

Abstract

At present, hydrofracture technology is mainly used for shale gas exploration and exploitation, and the effect of volume fracturing is tightly linked to the mechanical properties (including anisotropy and brittleness) of shale. Meanwhile, Sichuan Basin is also an important area for unconventional natural gas exploration and development in China. This work analyzed mineral composition and microstructure of outcrop shale matrix in Lower Silurian Longmaxi Formation through XRD test, slice observation, and scanning electron microscope (SEM). How anisotropy affects shale deformation, strength and failure characteristics at different bedding angles (0°, 30°, 45°, 60°, and 90°) under diverse confining pressures (0 MPa, 25 MPa, 50 MPa, 75 MPa, and 100 MPa) in conventional uniaxial/triaxial experiments were discussed. The acoustic emission (AE) evolution was introduced to reveal the cracks closure and propagation of Longmaxi Formation shale and qualitatively characterized the brittleness of the shale. What's more, based on the existing brittleness index, this study proposed an indicator BI_{new} that considers the shape of the stress–strain curve before and after the peak stress to evaluate the brittleness of the Longmaxi Formation shale. The index BI_{new} can better describe the changes of brittleness with confining pressure and bedding angle. Finally, this work elaborately explained the relationship between AE characteristics, brittleness, and failure modes of shale. AE characteristics can not only qualitatively characterize shale brittleness but also show the failure process and modes of shale samples. Change of failure modes rests with the difference in brittleness and also reflects the level of brittleness. The change of brittleness with failure modes can be expressed as shear along bedding plane (Sh-AI) > splitting through bedding plane (Sp-Th) > conjugate shear failure (Co-Sh) > shear along bedding plane (Sh-AI) > shear through bedding plane (Sh-Th).

Highlights

1. Uniaxial/triaxial compression and acoustic emission (AE) monitoring of Longmaxi formation shale were carried out.
2. Influence of anisotropy of shale on mechanical properties under different confining pressures was analyzed.
3. Different brittleness indexes were used to evaluate the brittleness of shale, and a new brittleness index was established.
4. Relationship between AE characteristics, brittleness, and failure modes of shale was discussed in detail.

Keywords Shale gas · Anisotropy · Brittleness index · Acoustic emission (AE) · Failure modes

✉ Jianfeng Liu
liujf@scu.edu.cn
Chengxing Zhao
zcxzcx182@163.com

- ¹ State Key Laboratory of Hydraulics and Mountain River Engineering, Sichuan University, Sichuan 610065, China
- ² College of Water Resource and Hydropower, Sichuan University, Sichuan 610065, China
- ³ CNPC Key Laboratory of Oil and Gas Underground Storage Engineering, Langfang 065007, China

1 Introduction

Shale gas mainly exists in organic shale and interlayers in a free or adsorbed state. As clean and efficient unconventional natural gas energy, shale gas plays an essential role in global energy development. Similarly, China also hopes to solve its energy problems through shale gas (Li et al. 2016b; Lin and Li 2020; Yuan et al. 2015b). China is abundant in shale gas reserves, and the recoverable shale gas resources in

favorable areas are 2.18×10^4 bcm, ranking first in the world (Weber and Clavin 2012), but the proven rate of shale gas is only 4.79% (Wei et al. 2021), indicating a huge potential for shale gas exploitation. However, compared with other countries such as the United States, shale gas in China is buried quite deeper. According to relevant data (Guan et al. 2014; Lee and Sohn 2014; Lin et al. 2013; Wei et al. 2021; Zhao et al. 2013), shale gas reserves buried deeper than 3500 m accounted for 65% of the total, and the average depth of shale gas in the Sichuan Basin is between 2957 and 4023 m; favorable mining areas with buried depth more than 3500 m in southern Sichuan accounted for over 82% of this area. Hydrofracture is widely used in shale gas exploration and development (Cheng et al. 2015; Lin et al. 2017; Ren and Lau 2020; Tan et al. 2017; Zhang et al. 2019a), but high crustal stress in the deep formation will severely affect the drilling stability and volume fracturing effect of shale reservoir or lead to problems such as collapse and the leakage of drilling wellbore (Chen et al. 2017; Liu et al. 2021; Yang et al. 2020). Therefore, exploring the mechanical properties of shale under high crustal stress is significant for the application and promotion of hydrofracture technology in shale gas production.

Due to internal bedding planes in shale, physical, mechanical, and hydraulic properties of shale are far from the same in different directions. Based on this, shale is considered to possess anisotropic mechanical properties. Making a clear understanding of shale anisotropy can provide a safety guarantee for exploring shale gas and maintaining shale gas drilling stability (Yang et al. 2020). Specifically, Hiroki et al. (2013) pointed out that the mechanical properties of different shale reservoirs or the same shale reservoir are significantly different, which is attributed to the diverse material compositions and microstructures of organic-rich shale. Niandou et al. (1997) conducted a triaxial compression test on Tournemire shale with different bedding angles. The test results illustrate that Tournemire shale shows anisotropic plastic deformation under triaxial compression and failure modes display obvious anisotropy, which is greatly affected by confining pressure and loading direction. Moreover, Kuila et al. (2011) studied stress anisotropy and anisotropy response of ultrasonic velocity of low-porosity shale in the Officer Basin and analyzed how ultrasonic velocity is affected by magnitude and direction of shale microfabric stress. Cho et al. (2012) conducted research that focus on the deformation and strength anisotropy characteristics of Asan gneiss, Boryeong shale, and Yeoncheon schist in Korea by uniaxial test and Brazilian Split test, finding that anisotropic mechanical properties of rock mass must be considered, avoid larger errors in rock engineering. A direct shear test was performed on shale samples with bedding angles of 0° , 30° , 60° , and 90° by Heng et al. (2015), who theoretically deduced an analytical formula for shear stress concentration

factor in the test, and proposed that shear strength of shale also displays obvious anisotropy. Under different confining pressures, temperatures, and strain rates, Rybacki et al. (2015) launched uniaxial and triaxial compression tests on black shales from Europe. The test results show the mechanical properties of shale vary with bedding angle and loading direction. Under the brittle state, the compressive strength of shale increases nonlinearly with the change of confining pressure, while shale will change from brittleness to semi-brittleness at higher temperature or confining pressure. Yang et al. (2019) stated that analysis of tensile strength and fracture modes of shale matter a lot for hydrofracture technology. Correspondingly, the Brazilian split test and PFC numerical simulation were used to explore the mechanical properties and failure modes of shale. According to tests, the Brazilian tensile strength of shale declines linearly with the change of dip angle, and shale matrix tensile fracture and shear fracture are the main failure modes in the Brazilian split test. Subsequently, Li et al. (2020) carried out uniaxial fatigue tests on shale of seven bedding angles under different loading frequencies and cyclic stress limits. Under influence of fatigue loading and bedding, cracks on shale samples will cross and interact with each other to eventually form a network of cracks. Acoustic emission (AE) technology was adopted by Wu et al. (2017), Ma et al. (2017) and Li et al. (2018) to monitor the failure process of shale under different stress levels and states, and they concluded that AE technology can directly reflect fracture regular of shale. What's more, Liu et al. (2021) investigated the anisotropic mechanical properties of shallow outcrop shale and deep shale through the uniaxial compression test and made a comparison of their mechanical properties. According to test results, Poisson's ratio and compressive strength of shale change in a U-shaped pattern with the bedding angle, and the compressive strength and elastic modulus of deep shale are smaller than those of shallow one. In addition, it should be noted that Ramamurthy (1993) classified the mechanical properties of rock into "shoulder shape, U shape, and wave shape" according to the change of bedding angle. Based on experimental data related to anisotropic rocks, many scholars had also proposed theoretical standards and numerical models to predict the strength of anisotropic rocks (Ashour 1988; Yao et al. 2016; Hoek 1980; Jaeger 1960; Mclamore and Gray 1967; Qi et al. 2016; Rao et al. 1986; Shao et al. 2015; Shi et al. 2016; Singh et al. 2015; Tien et al. 2006; Wang et al. 2020; Welemene et al. 2016; Wilson 2013; Yong and Ming 2001). These theories and numerical models can better predict the mechanical properties of anisotropic rocks. However, the above-mentioned related research on mechanical properties of shale anisotropy indicates that more experimental data are needed for verification of shale with inherent anisotropy. In particular, the anisotropy of shale should be discussed further under high confining pressure.

During shale gas production, anisotropy of shale impact drilling stability and volume fracturing effect, and besides that, brittleness also affects the productivity of shale gas (Hajiabodolmajid 2001). Under favorable crustal stress conditions, the shape and volume of the fracture zone are decided by the brittleness of shale. In other words, when shale is more brittle, and the fracture network in shale reservoir is deeper and more complex, the productivity of shale gas would be higher. Therefore, analysis of shale brittleness is critical for shale gas production (Chandler et al. 2013; Rybacki et al. 2016; Zhang et al. 2016). The brittleness index (BI) is commonly used to evaluate rock brittleness. However, there is no clear definition for the measurement and calculation of BI. Numerous scholars listed brittleness indexes to quantify the strength of rock brittleness (Altindag 2002; Barnhoorn et al. 2016; Hucka and Das 1974b; Huo et al. 2018; Li et al. 2016a; Runar et al. 2006; Yagiz 2009; Yuan et al. 2015a; Zou et al. 2021), but due to different definitions, measurement, and calculation methods of brittleness indexes, even if brittleness of the same rock is assessed, greatly different BI values will be caused (Yang et al. 2013). Geng et al. (2016) proposed that brittleness essentially means that rocks are broken suddenly without severe plastic deformation under stress. For shale, it has inherent anisotropic properties, and brittleness performance is also directional (Martin et al. 2011), which was confirmed by research on anisotropic shale brittleness after Rune et al. (2015). Similarly, in the laboratory test, the brittleness of rock not only displays anisotropy, and is also affected by the change of confining pressure. The brittleness of rock samples is in a ductile trend under high confining pressure, but stronger under low confining pressure, indicating that the mechanical properties of shale samples are dramatically affected by different stresses. As a result, the mechanical parameters of rock samples should be considered when defining BI to evaluate rock brittleness in laboratory tests. It specifically includes elastic properties (elastic modulus, Poisson's ratio, etc.), strength parameters (compressive strength, shear strength, tensile strength, etc.), energy evolution (elastic energy, dissipation energy, etc.), strain (elastic strain, plastic strain, residual strain, etc.), and fracture toughness, etc. (Barnhoorn et al. 2016; Bi et al. 2020; Geng et al. 2016; Huo et al. 2018; Yuan et al. 2015a; Zou et al. 2022). In many studies, the triaxial compression test was launched to analyze the variation of shale brittleness index (BI) under different confining pressures (Amann et al. 2012; Arora and Mishra 2015; Guo et al. 2020; Lawal and Mahmoud 2020; Ren et al. 2018; Yang et al. 2021; Yi et al. 2016). Unfortunately, there are limitations for bedding angle change and confining pressure range of shale in most experiments, so that they cannot reflect the change of BI under high confining pressure, and only provide limited

guidance on adopting hydrofracture to develop shale gas in deep shale formations.

In conclusion, this work mainly analyzes outcrop shale samples of the Lower Silurian Longmaxi Formation in Changning, Sichuan Basin, China. The composition and microstructure of intact shale sample matrix were explored by XRD test, slice observation, and scanning electron microscope (SEM), followed by conventional uniaxial/triaxial compression tests to investigate the deformation and failure of shale samples at different bedding angles (0°, 30°, 45°, 60°, and 90°) under different confining pressures (0 MPa, 25 MPa, 50 MPa, 75 MPa, and 100 MPa). Meanwhile, the anisotropy (including deformation, damage, and strength) of shale under different confining pressures and bedding angles were revealed. Acoustic emission (AE) technology was applied to monitor the whole process of deformation and failure of shale samples in conventional triaxial compression tests, and the AE characteristics in the deformation and failure process of shale were analyzed. Furthermore, the brittleness of shale samples under different confining pressures and bedding angles was evaluated using a variety of brittleness indexes (BI). Finally, the relationship between shale brittleness, AE characteristics, and failure modes was discussed in detail. The research results are hoped to provide a reference for shale gas exploitation by hydrofracture technology under high crustal stress.

2 Preparation and Characterization of Shale Samples

2.1 Shale Sampling Location and Its Geological Characteristics

According to relevant data (Wei et al. 2021; Zhao et al. 2013), Sichuan Basin is a key unconventional natural gas exploration area in China. The Longmaxi Formation shale in this area is thick and widely distributed, with abundant shale gas resources, and shale gas reserves account for 66% of the total reserves of the nation. Therefore, it is significant for China's oil and gas exploration through studying the Longmaxi shale in this area. In this study, the Longmaxi shale samples were collected from an outcrop shale in Shuanghe Town, Changning, Sichuan Province, China (Fig. 1). Thanks to construction and excavation, sampling there is extremely convenient, and there are a large number of fresh and complete outcrop shales. Meanwhile, three basic requirements must be followed during field sampling, to ensure the integrity and uniformity of shale samples during the test (Yang et al. 2020):

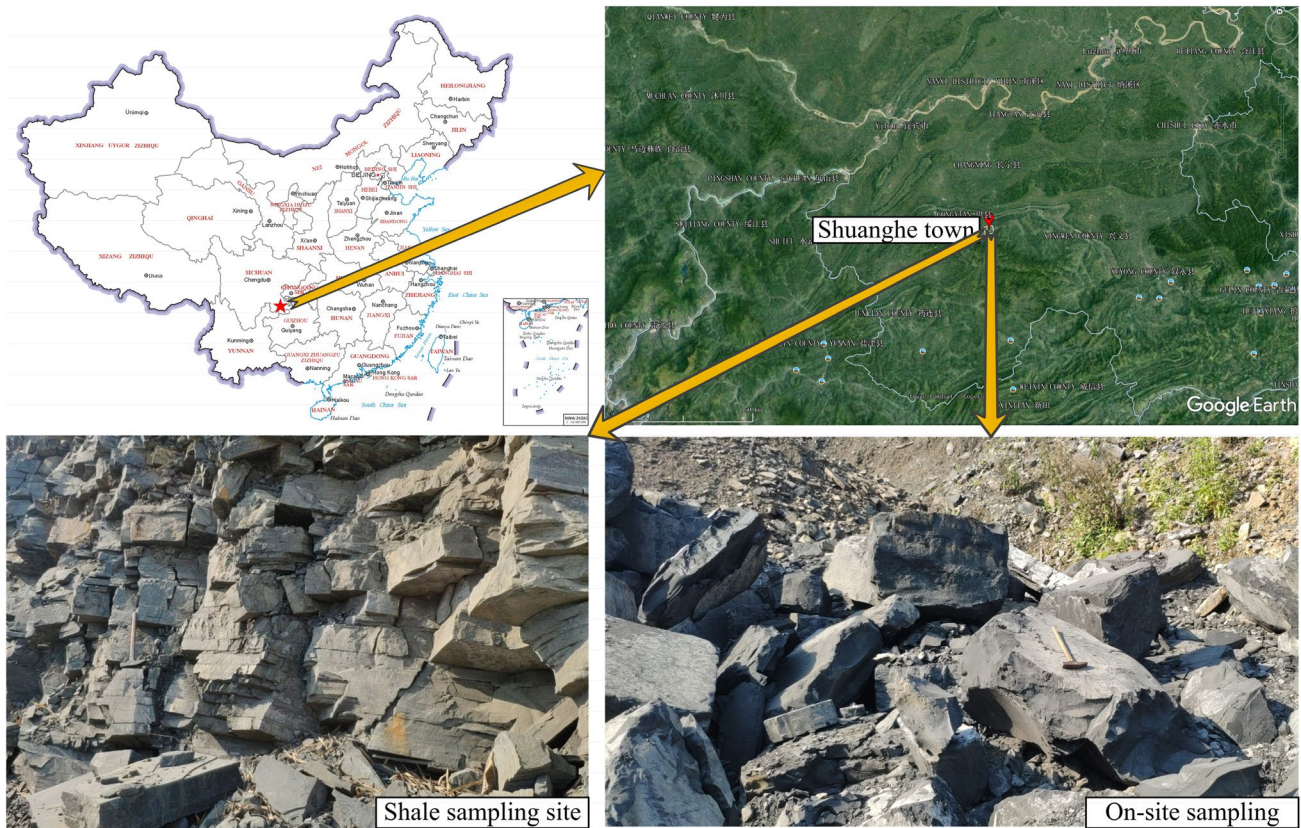


Fig. 1 Longmaxi shale sampling site

1. Shale blocks taken on site can be placed horizontally, and bedding must be visible; bedding of shale blocks can be kept horizontal when blocks are laid flat, which facilitates the preparation of standard shale samples with different bedding angles in subsequent laboratory tests.
2. The size of shale blocks should be within a reasonable range, to facilitate transportation and processing, and ensure the number of standard shale samples required for the experiment.
3. When shale blocks are prepared on-site, there should be no cracks and pores on the blocks, to ensure the integrity of shale blocks.

Shale at the sampling site is marine black rock (Fig. 2), rich in biological fossils and organic matter, with clear bedding development, which belongs to Paleozoic Low Silurian Longmaxi Formation. After shale blocks were taken on site, the dip angle was changed according to the method in Fig. 3, to change the angle between the bedding plane and the horizontal plane, and prepared cylindrical rock samples with different bedding angles (0° , 30° , 45° ,



Fig. 2 Outcrop rock blocks taken from the sampling site

60° , and 90°). The α is the angle between the bedding plane and the horizontal plane of shale samples. International Society for Rock Mechanics (ISRM) emphasized that the height–diameter ratio of rock samples used for rock mechanics tests should be kept between 2.0–3.0 (Fairhurst and Hudson 1999; Hatheway, 2009; Lyu et al.

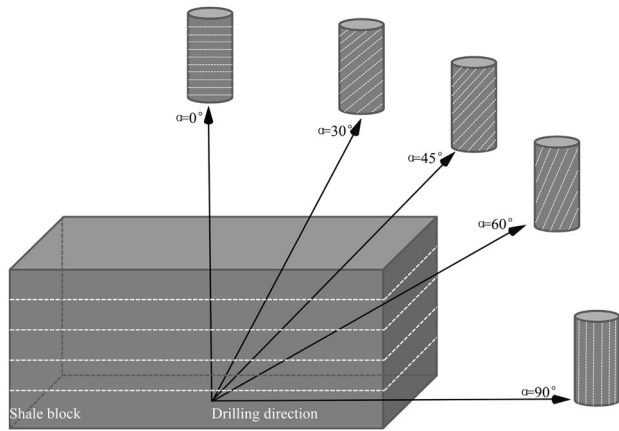


Fig. 3 Preparation method of shale specimens with different bedding angles

2021a), to minimize the influence of end friction on results during the test. Hence, the cylindrical rock samples were processed into standard cylindrical specimens with a diameter of 50 mm and height of 100 mm, as shown in Fig. 4. In addition, all shale samples were placed in a dry environment at room temperature, and the test was completed within 30 days, to guarantee the accuracy and reliability of experimental results.

2.2 Mineral Composition and Microstructure Analysis

Making a clear understanding of the mineral composition and microstructure of shale is critical to evaluating shale reservoirs, which impose a profound impact on the occurrence and migration of shale gas, as well as the shape and diffusion path of hydraulic fractures. Furthermore, brittleness is a key factor affecting the hydraulic fracturing effect, and in terms of the mineral composition of shale, brittleness is influenced by the proportion of quartz (Amann et al. 2012; Yang et al.

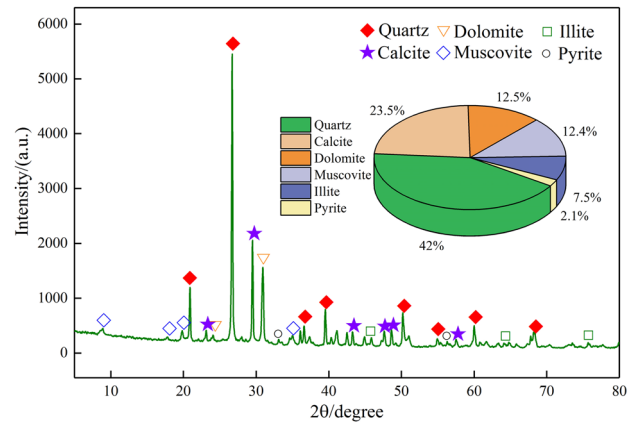


Fig. 5 Mineral composition and proportion of shale samples

2020), the larger the proportion of quartz, the higher the brittleness. Of course, lots of rock core powder was collected during the process of specimen drilling and an XRD test was launched, as shown in Fig. 5.

According to XRD test results, the shale used in this experiment mainly contains quartz, calcite, dolomite, muscovite, illite, and pyrite. Among them, quartz and calcite account for 65.5%; quartz has the largest proportion in the mineral composition, as high as 42%, and the content of pyrite is lower, only 2.1%. To better understand the composition and microstructure of shale samples, this study identified slices of shale samples and conducted SEM scanning. The shale samples were first made into rock slices of 25 mm * 20 mm * 0.05 mm and then observed with a polarizing microscope in the direction perpendicular to the bedding plane. The identification results of slices are introduced in Figs. 6, and 7 is the SEM image of the complete shale surface. It can be seen from Figs. 6 and 7 that the shale samples have an obvious bedding structure. Figure 6 shows lots of carbon-argillaceous minerals with weak light visibility are uniformly distributed in shale samples, and white minerals

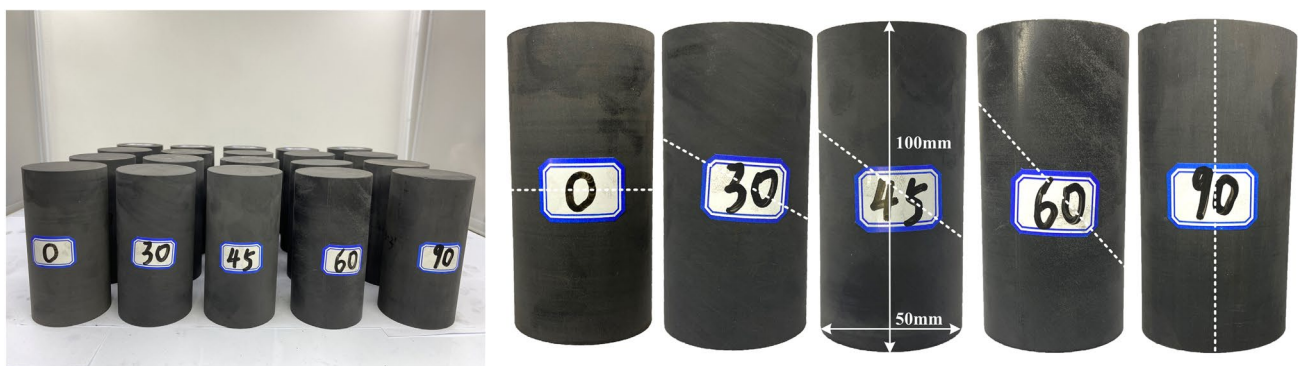


Fig. 4 50 mm × 100 mm standard cylindrical shale specimens

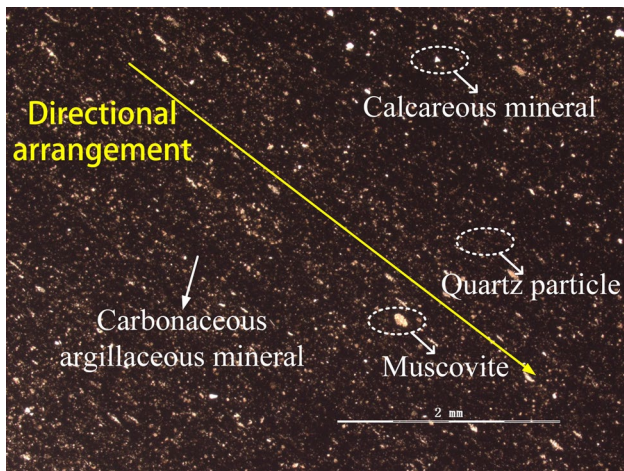


Fig. 6 Identification of shale thin sections

such as quartz, muscovite, and calcareous minerals are arranged in a directional arrangement. In Fig. 7, lamelliform minerals are in obvious directional alignment and some scattered calcium mineral particles such as quartz are found. Due to lamelliform minerals, shale samples selected for this experiment possess inherent anisotropy. Along the bedding direction, on the boundary of lamelliform minerals are also pores and micro-fractures that are not only original defects inside the shale samples but also the main place for shale gas occurrence and migration.

3 Experimental Apparatus and Testing Procedure

This experiment aims to analyze mechanical properties, AE characteristics and failure modes of Longmaxi Formation shale in Changning, Sichuan Province, China. The MTS815 Flex Test GT rock mechanics system of Sichuan University was selected for conventional uniaxial/triaxial compression

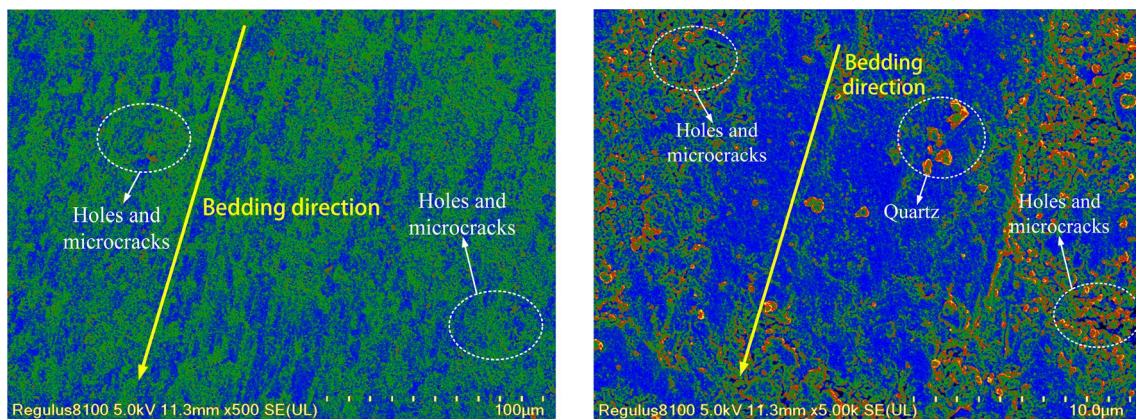


Fig. 7 Microstructure of intact shale samples (pseudo-color map)

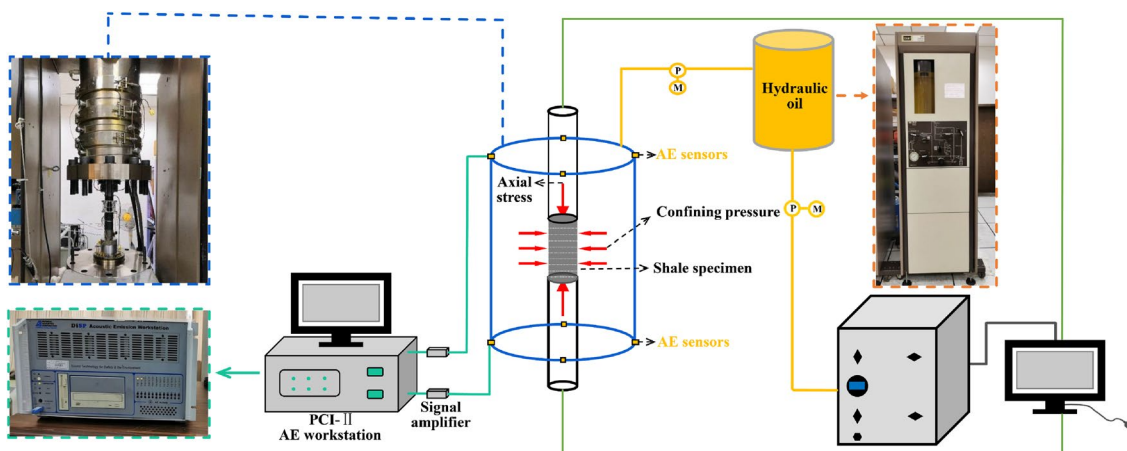


Fig. 8 MTS815 rock mechanics test system

tests, and the PCI-2 acoustic emission three-dimensional positioning system was introduced to monitor the deformation and failure process of shale, as shown in Fig. 8. The maximum axial load of the system can reach 4600 kN, with maximum confining pressure of 140 MPa. The axial deformation and circumferential deformation of rock samples was measured by axial and hoop extensometers, respectively. In the uniaxial compression test, the measurement range of the axial extensometer is $-4\sim 4$ mm, and that of the hoop extensometer is $-2.5\sim 8$ mm. Similarly, in the triaxial compression test, the measurement range of the axial extensometer is $-5\sim 5$ mm, and that of hoop extensometer is $-2.5\sim 15$ mm, with all accuracy of 5% (Lyu et al. 2021b; Zhou et al. 2019). The corresponding sampling rate of the PCI-2 acoustic emission three-dimensional positioning system was fixed at 40 MSPS; the gain of the corresponding amplifier was 40 dB, and the signal acquisition threshold was 30 dB. The whole test process would be controlled by a computer, and the system automatically recorded the axial stress, confining pressure, axial deformation, and hoop deformation of shale specimen during the loading process (Lyu et al. 2022; Zhang et al. 2019b).

The uniaxial compression test of shale samples with different bedding angles (0° , 30° , 45° , 60° , and 90°) can be carried out as per the following steps: First, applied axial stress at a rate of 30 kN/min; applied axial load with a hoop deformation rate of 0.02 mm/min at the end of the elastic deformation stage of shale samples; after the peak stress, continuously applied axial load at a hoop deformation control rate of 0.04 mm/min, which eventually damaged rock samples. Similarly, the process of triaxial compression test of shale samples with different bedding angles (0° , 30° , 45° , 60° , and 90°) under different confining pressures (25 MPa, 50 MPa, 75 MPa, and 100 MPa) is as follows: increased confining pressure to a predetermined value (the rate of increase of confining pressure must be slow enough to ensure the integrity of shale sample) at the rate of 3 MPa/min, and then applied axial stress at a rate of 30 kN/min. Just like the uniaxial compression test, the axial load was applied with a hoop deformation rate of 0.02 mm/min at the end of the elastic stage. After peak stress was reached, to adapt to the rapid and large circumferential deformation of the rock sample after the peak, the circumferential deformation control rate was increased to 0.04 mm/min and 0.10 mm/min to apply the axial load, and finally reached the residual stage (Lyu et al. 2021b). Before the experiment, the shape and quality of shale samples were measured and recorded, and these samples were kept dry and tested at room temperature, to ensure accurate test results.

4 Experimental Results and Discussion

4.1 Analysis of Mechanical Properties of Longmaxi Formation Shale

4.1.1 Characteristics of Stress–Strain Curves

Figure 9 describes the stress–strain curves of shale samples under different confining pressures (due to limited space, only the stress–strain curves of shale at bedding angles of 0° , 30° , 45° , and 90° are given). Figure 10 shows the stress–strain curves of shale samples under different bedding angles (only the stress–strain curves of shale under confining pressures of 0 MPa, 25 MPa, 75 MPa, and 100 MPa are given). In general, the stress–strain curves of Longmaxi shale are significantly different from those of granite, sandstone, and halite (Li et al. 2018; Nishiyama et al. 2002; Wang et al. 2018). Because of the low-porosity and dense structure of shale, the stress–strain curves are free of obvious microcracks compaction stage of shale in triaxial compression, and it mainly goes through four stages, such as near-linear elastic deformation stage I, bedding activation and stable microcracks' propagation stage II, bedding initiation slip and unstable microcracks propagation stage III, bedding severely slips and post-peak failure stage IV. In the triaxial compression experiment, because the large microcracks and weak bedding planes in the shale matrix have been highly compacted and closed in process of increasing confining pressure to target confining pressure, the shale matrix and bedding are compressed in the initial stage of applying axial load. Once compressed, the shale will enter the near-elastic deformation stage (elastic modulus E and Poisson's ratio μ are determined by the stress–strain relationship of shale in this stage). As deviatoric stress increases to cracks initiation stress σ_{ci} (Fig. 11), cohesion between internal bedding and matrix of the shale weakens, the bedding is activated, and microcracks begin to expand stably. At the same time, shale no longer shows typical linear elastic characteristics, and the stress–strain curves change from straight to curved; shale enters bedding activation and stable microcracks' propagation stage II under the axial load and confining pressure. When deviatoric stress continues to increase to cracks damage stress σ_{cd} (Fig. 11), microcracks in the shale increase gradually, causing bedding to slip, and volume expansion of shale samples. The cracks damage stress σ_{cd} corresponds to the dilatancy point (Fig. 11), which also marks shale samples entering the stage of bedding initiation slip and unstable microcracks propagation. At this stage, shale samples will experience a certain plastic deformation under the axial load and confining pressure. Figure 9 demonstrates that most shale samples produce

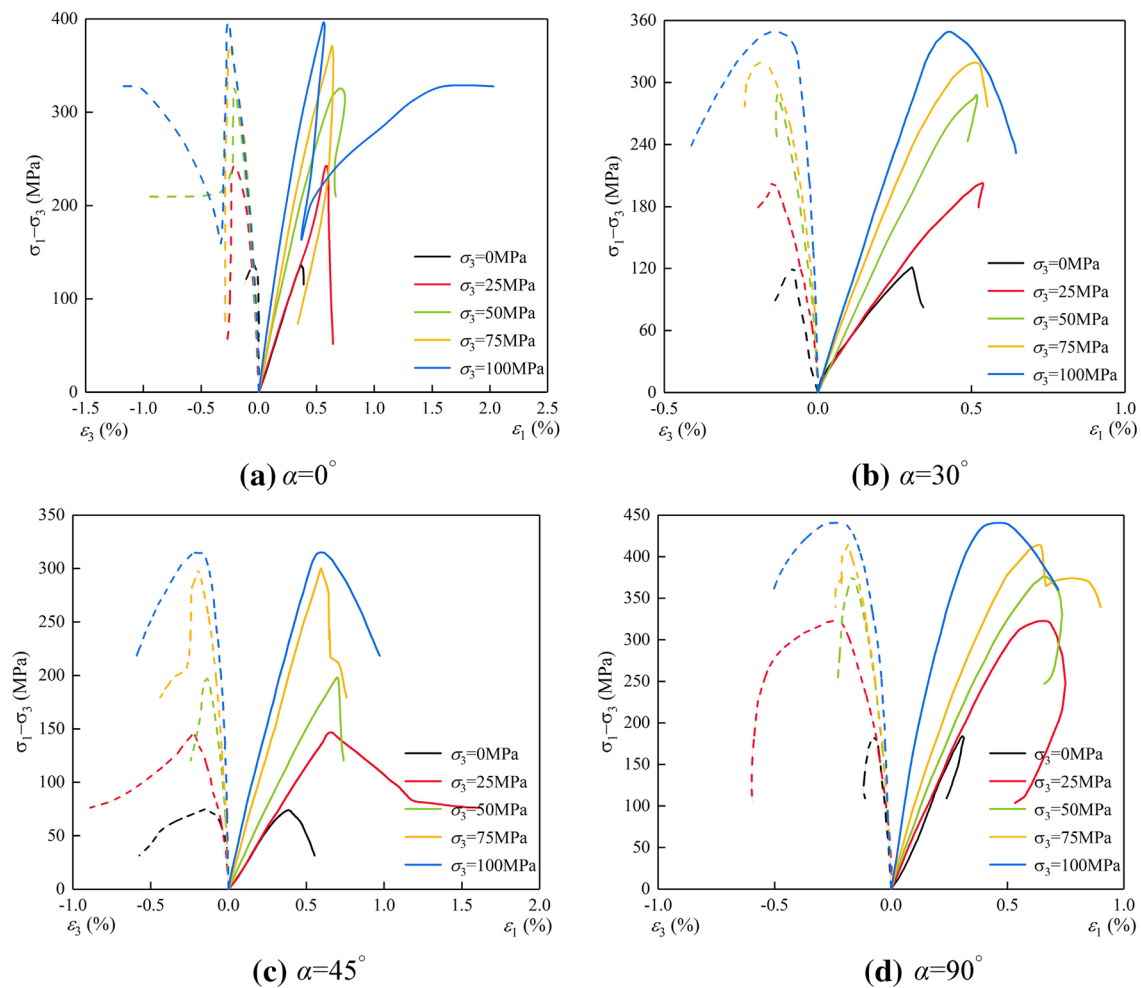


Fig. 9 Stress–strain curves of shale samples under different confining pressures σ_3

small plastic deformation before peak stress and reach peak stress σ_f in a “sharp” form (Yang et al. 2020), indicating the strong brittleness of shale samples in this experiment. After deviatoric stress reaches the peak stress σ_f , shale samples enter the bedding severely slips and post-peak failure stage IV. In this stage, the bedding of shale samples slips violently and forms a through tension or shear failure surface; deviatoric stress drops sharply, and a crisp failure sound often occurs during shale samples failure, implying that the shale samples show strong brittle failure characteristics, as shown in Fig. 9.

Additionally, Fig. 9 shows that the failure strength of shale is greatly affected by confining pressure, and the higher the confining pressure, the greater the peak stress. The relationship between the forms of stress–strain curve and brittleness is explained in Fig. 12. The higher the brittleness, the stress–strain curve will be accompanied by the decrease of axial strain while the peak stress drops, which signifies the unstable failure of shale. A comparison between Figs. 9 and 12 indicates that with the increase of confining pressure,

stress after the peak gradually slows down with the decreasing trend of axial strain, and the brittle failure characteristics gradually weaken. In Fig. 10, shale with different bedding angles has various mechanical properties even under the same confining pressure. A significant change is found in elastic modulus E and peak stress σ_f with the bedding angle, showing that the shale samples have obvious anisotropy. Interestingly, according to the forms of stress–strain curves, anisotropy is found in the brittleness of shale. Under the confining pressure of 0 MPa, the stress of shale with the bedding angle of 60° declines more slowly after the peak stress σ_f , and brittleness is lower. At 25 MPa confining pressure, the brittleness of shale is lower at the 45° bedding angle.

4.1.2 Deformation and Strength Characteristics of Longmaxi Formation Shale

The aforementioned analysis of stress–strain curves indicates that the Longmaxi Formation shale has obvious anisotropy, and the changes in confining pressure

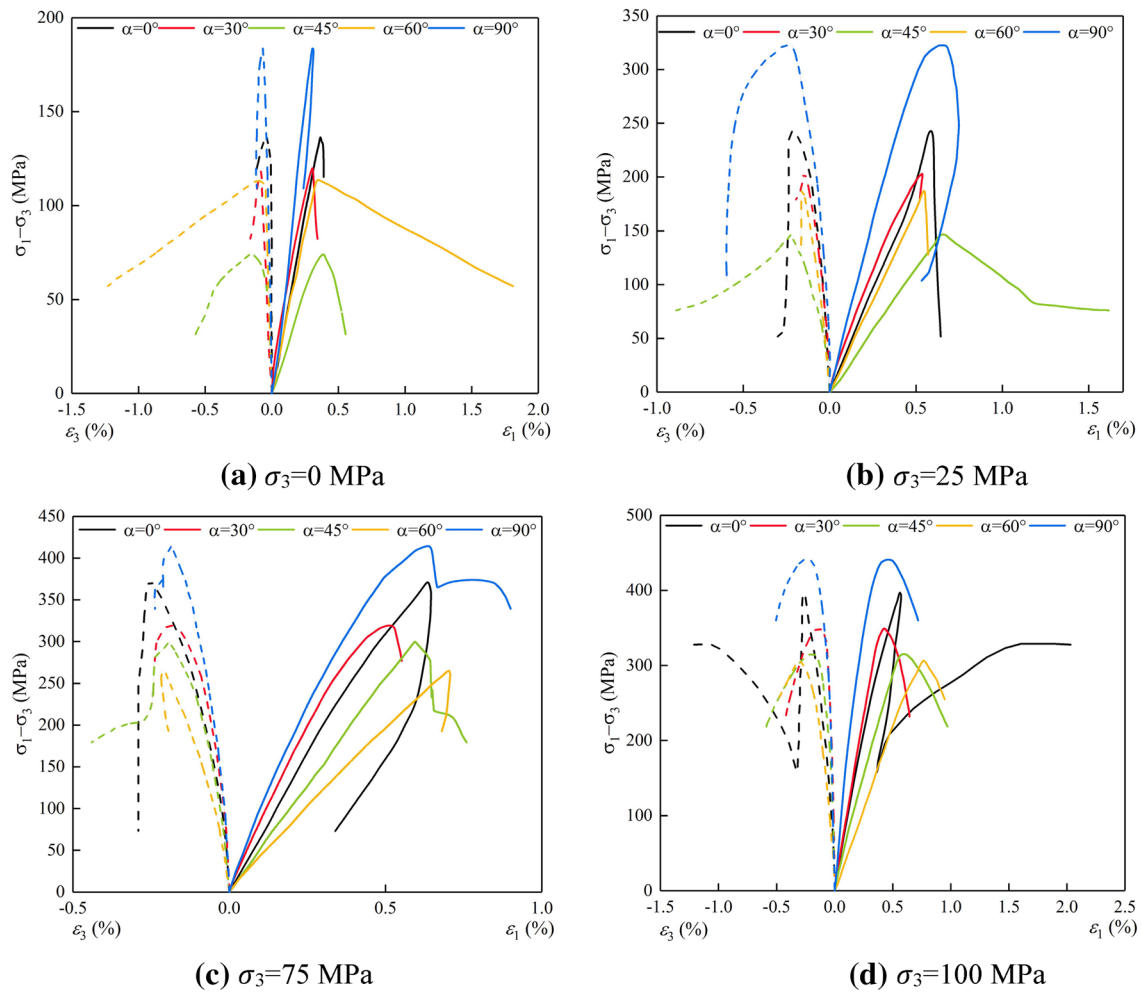


Fig. 10 Stress–strain curves of shale samples under different bedding angles α

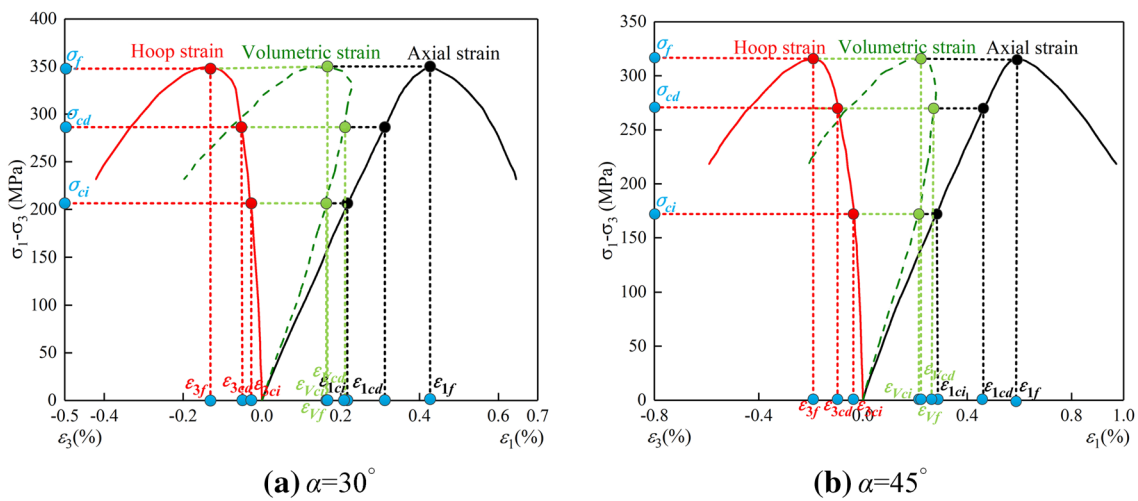


Fig. 11 Typical stress–strain curves of shale under triaxial compression (take shale sample with 30° and 45° bedding angle under 100 MPa confining pressure as example)

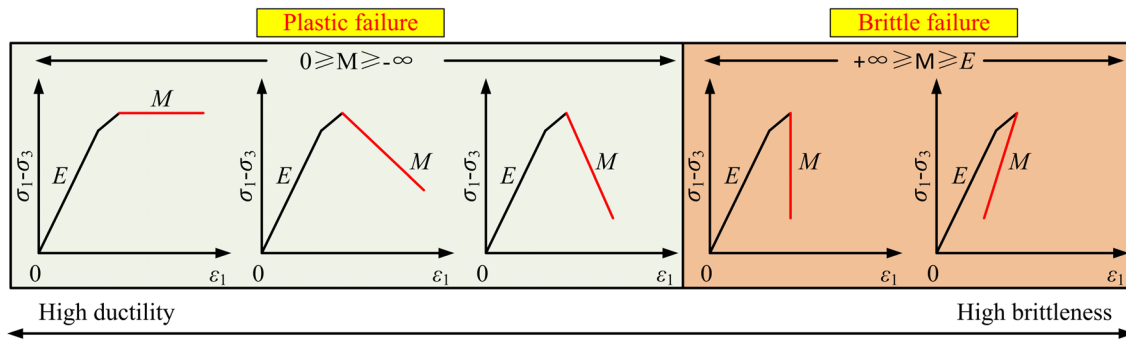


Fig. 12 Relationship between stress–strain curve forms and brittleness (Tarasov and Potvin 2013)

and bedding angle produce a significant impact on its mechanical properties. This part will discuss the deformation failure and strength characteristics of Longmaxi Formation shale in light of stress–strain curves (Figs. 9, 10). Figure 13 introduces how elastic modulus E , Poisson's ratio μ , axial cracks initiation strain ε_{1ci} , axial cracks damage strain ε_{1cd} , axial peak strain ε_{1f} , cracks initiation stress σ_{ci} , cracks damage stress σ_{cd} , peak stress σ_f of Longmaxi Formation shale change with bedding angle α . In Fig. 13a,b, the distribution of Poisson's ratio μ is relatively discrete and changes less with confining pressure and bedding angle. However, the elastic modulus E increases continuously with the rise of confining pressure and changes in a “U”-shaped pattern as the bedding angle increases from 0° to 90° . Since the bedding plane of shale samples with a bedding angle of 90° is parallel to the squeezing direction, most specimens are fractured along the bedding plane, and the sedimentary compaction degree of samples is high. Therefore, the elastic modulus E obtains the maximum value at $\alpha = 90^\circ$ under different confining pressures. Furthermore, the elastic modulus E is the minimum at the position with $\alpha = 45^\circ$ under low confining pressures ($\sigma_3 = 0$ MPa, 25 MPa, 50 MPa), and at the position with $\alpha = 60^\circ$ under high confining pressures ($\sigma_3 = 75$ MPa, 100 MPa). Meanwhile, a lower elastic modulus E will lead to a larger peak strain ε_{1f} (Yang et al. 2020). The peak strain ε_{1f} changes dramatically with bedding angle, and its change pattern corresponds to the elastic modulus E each other, as shown in Fig. 13e. Under low confining pressure, peak strain ε_{1f} has the maximum value at the position with bedding angle $\alpha = 45^\circ$; under high confining pressure, the maximum value is found at the position with bedding angle $\alpha = 60^\circ$. Coincidentally, it shows from Fig. 13c, d that the variation pattern of axial cracks initiation strain ε_{1ci} and axial cracks damage strain ε_{1cd} with bedding angle α is consistent with that of axial peak strain ε_{1f} with bedding angle α . Under the same confining pressure, axial cracks' initiation strain ε_{1ci} changes with the bedding angle smaller than that of axial cracks damage strain ε_{1cd} and

axial peak strain ε_{1f} with a maximum difference of only 1.87×10^{-3} , and the maximum difference of axial damage strain ε_{1cd} with the bedding angle α is 2.84×10^{-3} , which indicates that the initiation of new cracks in shale matrix is less affected by bedding angle than that in the propagation process. After cracks initiation, the microcracks will expand under the continuous loading of axial stress. When it expands to intersect with the bedding plane, the properties of the bedding plane (angle, strength, etc.) will exert an influence on propagation direction, scope, degree of intersection, and connection, which is the reason why cracks damage stress σ_{cd} and peak stress σ_f in Fig. 13g, h change drastically with the bedding angle α , showing strong anisotropy.

Figure 13h shows that under the same bedding angle, as confining pressure rises, peak stress σ_f also increases, signifying that the confining pressure can improve shale strength. Under the same confining pressure, peak stress σ_f of shale is in a changing pattern of “decrease first and then increase” with the increase of bedding angle. The shale matrix is uniformly stressed under the bedding angle of 0° and 90° , and the peak stress σ_f is larger and close. Under low confining pressures ($\sigma_3 = 0$ MPa, 25 MPa, 50 MPa), peak stress σ_f is the minimum at the position with bedding angle $\alpha = 45^\circ$, and shale sample is more easily damaged by bedding structure at 45° bedding angle. However, under high confining pressures ($\sigma_3 = 75$ MPa, 100 MPa), shale has the lowest compressive strength at the position with bedding angle $\alpha = 60^\circ$, and the shale sample is more easily damaged by the influence of bedding structure at 60° . This shows the influence of bedding angle on shale strength changes with the increase of confining pressure. The “dangerous bedding angle” will increase from 45° to 60° in the process of increasing from low to high confining pressure, which is also a unique performance of anisotropy of shale when low confining pressure rises to high confining pressure.

To analyze the strength characteristics of Longmaxi formation shale, according to the Mohr–Coulomb strength criterion (Cai et al. 2022; Labuz and Zang 2012), the

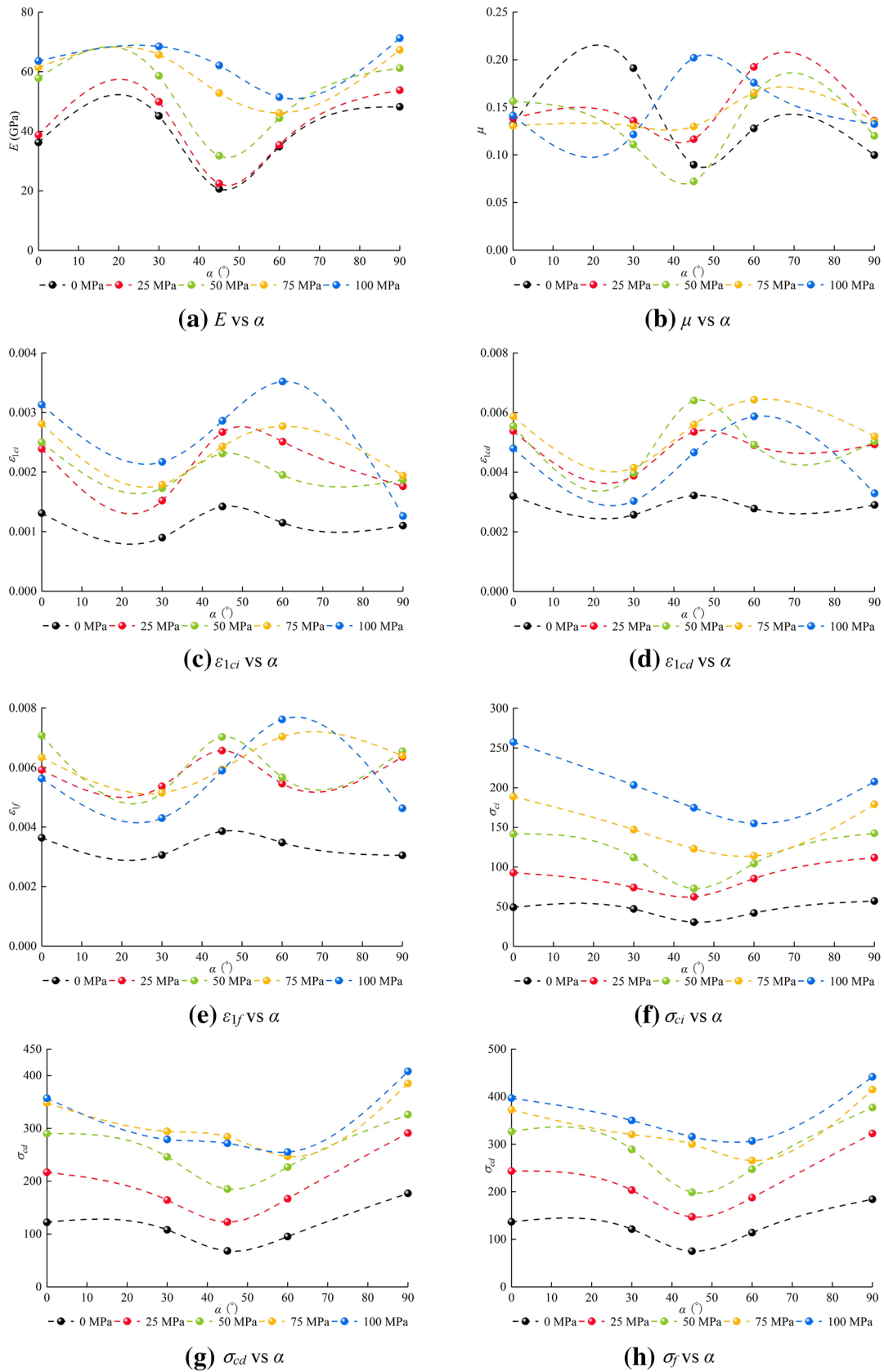


Fig. 13 Variation of deformation and strength parameters of shale with bedding angle α



Fig. 14 Variation of cohesion c and internal friction angle φ with bedding angle α

relationship between the maximum principal stress σ_1 and the minimum principal stress σ_3 of Longmaxi formation shale can be expressed as follows:

$$\sigma_1 = \frac{1 + \sin \varphi}{1 - \sin \varphi} \sigma_3 + \frac{2 \cos \varphi}{1 - \sin \varphi} c, \tag{1}$$

where φ represents the internal friction angle; c is the cohesion of shale sample.

Therefore, the compressive strength of shale samples with the same bedding angle under different confining pressures is fitted to obtain the linear relationship between the maximum principal stress σ_1 and the minimum principal stress σ_3 , and then, the cohesion c and internal friction angle φ of shale sample under different bedding angles are calculated according to Eq. (1), as shown in Fig. 14. The cohesion c can be expressed as shear strength on failure surface under normal stress, which affects the shear resistance of rock samples. As can be seen from Fig. 14, the variation of cohesion c

with bedding angle α is consistent with the change mode of peak strength σ_f and also shows the trend of “first decreasing and then increasing” with the increase of bedding angle, but the internal friction angle φ changes insignificantly with the bedding angle as a whole, with average value about 33.51°. It should be noted that cohesion c has the maximum at the bedding angle of 90°, and minimum at bedding angles of 45° and 60°, which indicates that it is easy for shear cracks to propagate along with bedding angles of 45° and 60°, and eventually lead to shear slip failure of shale samples with 45° and 60° bedding angles.

To quantify the effects of bedding angle and confining pressure on strength of shale, the relative strength R_σ , anisotropy of compressive strength D_σ , and elastic modulus D_E are defined as follows (Niandou et al. 1997; Zhai et al. 2021b):

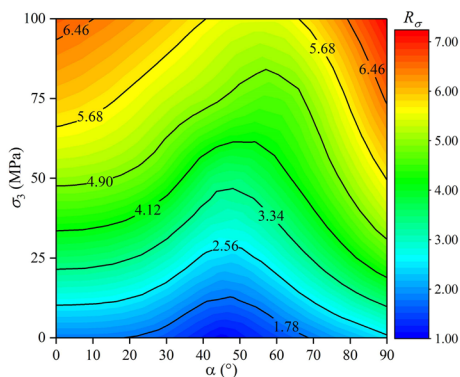
$$R_\sigma = \frac{\sigma_{1\theta}}{\sigma_{1\min}}, \tag{2}$$

$$D_\sigma = \frac{\sigma_{\max}}{\sigma_{\min}}, \tag{3}$$

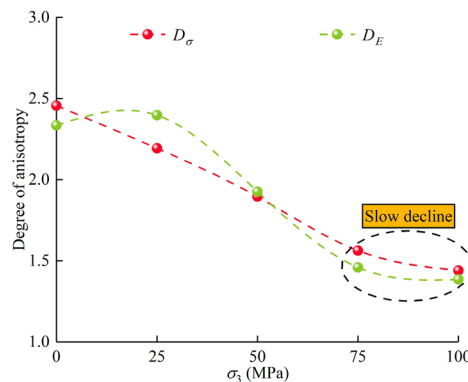
$$D_E = \frac{E_{\max}}{E_{\min}}, \tag{4}$$

where $\sigma_{1\theta}$ represents the first principal stress of shale sample under different confining pressures; $\sigma_{1\min}$ is the minimum first principal stress; σ_{\max} and σ_{\min} refer to the maximum and minimum compressive strength of shale samples with different bedding angles under the same confining pressure, respectively; E_{\max} and E_{\min} are expressed as the maximum and minimum elastic modulus of shale samples with different bedding angles under the same confining pressure, respectively.

Accordingly, the variety of relative strength R_σ , anisotropy of compressive strength D_σ and elastic modulus D_E is



(a) Relative strength R_σ .



(b) Anisotropy of compressive strength and elastic modulus.

Fig. 15 Variation of relative strength R_σ , anisotropy of compressive strength D_σ and elastic modulus D_E

obtained, as shown in Fig. 15. Due to the compaction effect of confining pressure on the microcracks and pores and its inhibition of the deformation and failure of shale samples, the failure modes of shale samples will change. As a result, at the same bedding angle, relative strength R_σ increases when confining pressure rises from 0 to 100 MPa, while anisotropy of compressive strength D_σ decreases from 2.45 to 1.44, and that of elastic modulus D_E reduces to 1.38 from 2.33. This phenomenon implies confining pressure is beneficial to enhancing the compressive strength of shale and reducing anisotropy (Duveau et al. 1998). Furthermore, it can be seen from Fig. 15b that under high confining pressures ($\sigma_3 = 75$ MPa, 100 MPa), the effect of confining pressure on anisotropy is weakened, but shale still displays obvious anisotropy. Consequently, the anisotropy of shale should not be ignored when hydrofracture technology is used to exploit shale gas in deep shale formations. Otherwise, there will be large errors in fracturing geometric parameter design and fracturing effect prediction.

As mentioned previously, the Mohr–Coulomb criterion can describe the linear behavior of isotropic rock strength but affected by mineral composition and structure of shale, the strength is usually in a nonlinear variation pattern. The Hoek–Brown criterion has been widely applied to explain the nonlinear change of rock strength, with the basic equation as follows (Brown 1997; Hoek 1980):

$$\sigma_1 = \sigma_c \left(s + m \frac{\sigma_3}{\sigma_c} \right)^{0.5} + \sigma_3, \quad (5)$$

where σ_1 and σ_3 are the first principal stress and third principal stress, respectively; σ_c represents the compressive strength of the intact rock in uniaxial compression test. The s and m refer to correlation coefficients representing integrity and hardness of rock samples, respectively. The value of s ranges from 0 to 1, and the closer to 1, the more complete the rock samples. Because each shale sample is kept intact in this experiment, the value of s is 1. In addition, the harder the rock, the greater the value of m . The experimental data of shale obtained in the triaxial compression test are substituted into Eq. (5), to obtain parameter m under different confining pressures and bedding angles, as shown in Table 1.

To better describe and predict strength variation and mechanical properties of transversely isotropic rocks, such as shale, scholars proposed diverse anisotropic criteria (De et al. 1950; Jaeger 1960; Lee and Pietruszczak, 2008; Pietruszczak and Mroz 2001; Tsai and Wu 1971), which can be divided into continuous mathematical criteria, discontinuous empirical criteria, and continuous empirical criteria. In this paper, three classical anisotropic criteria are selected from these three types of criteria to evaluate the accuracy and adaptability of the uniaxial/triaxial experimental data of

Table 1 Relevant parameters of shale samples under different strength criteria

α (°)	0°	30°	45°	60°	90°
Mohr–Coulomb					
c	41.35	39.07	25.69	33.21	57.12
φ	36.84	32.32	34.01	30.76	36.47
R^2	0.9651	0.9715	0.9835	0.9795	0.9399
Hoek–Brown					
m	11.2809	9.5728	7.1669	7.3065	10.1403
s	1	1	1	1	1
R^2	0.9916	0.9922	0.9746	0.9944	0.9654
Nova					
a	1.2758	1.5692	1.6769	1.4584	1.5348
b	1.1989	1.2170	2.2000	1.4957	2.2649
c_{\min}	64.9024	61.1862	53.6965	38.9685	56.7129
γ_{\min}	2.2907	2.0458	1.9389	2.0105	1.1755
R^2	0.9922	0.9884	0.9853	0.9959	0.9720
Jaeger					
c_0	41.35	41.35	–	–	–
φ_0	36.84	36.84	–	–	–
c_{90}	–	–	–	–	57.12
φ_{90}	–	–	–	–	36.47
c_w	–	–	28.8823	34.9047	–
φ_w	–	–	32.63	31.9808	–
R^2	0.9651	0.9377	0.9823	0.9796	0.9399
Saeidi					
I	7.9546	6.2357	6.1270	6.4881	12.9548
J	1.7853	1.3169	0.6419	1.7011	4.3647
η	1.0123	0.9189	0.7171	1.0827	0.9973
R^2	0.9985	0.9959	0.9867	0.9965	0.9995

shale, and compared with the Mohr–Coulomb criterion and Hoek–Brown criterion. Based on the Mohr–Coulomb criterion, Nova (1980) analyzed the anisotropy of shale under the true triaxial stress state using tensor expressions and raised the anisotropic strength criterion suitable for the true triaxial stress state, which is a typical continuous mathematical criterion. The rock will fail when principal stress satisfies any of the followings:

$$\left| \frac{\sigma_1 - \sigma_3}{2} \right| = \left| [(f_{11} + c_{11})(f_{33} + c_{33})]^{0.5} - |f_{13} + c_{13}| \right|, \quad (6)$$

$$\left| \frac{\sigma_1 - \sigma_2}{2} \right| = \left| [(f_{11} + c_{11})(f_{22} + c_{22})]^{0.5} - |f_{12} + c_{12}| \right|, \quad (7)$$

$$\left| \frac{\sigma_2 - \sigma_3}{2} \right| = \left| [(f_{22} + c_{22})(f_{33} + c_{33})]^{0.5} - |f_{23} + c_{23}| \right|, \quad (8)$$

where \mathbf{f} and \mathbf{c} refer to the second-order tensor related to the internal friction angle φ and cohesion c , respectively. When

rock shows isotropy, the above formulas can be directly transformed into the Mohr–Coulomb failure criterion. For transversely isotropic rock such as shale, when the minimum friction coefficient γ_{\min} , the maximum friction coefficient $a\gamma_{\min}$, the minimum cohesion c_{\min} , and the maximum cohesion bc_{\min} are introduced, the Nova criterion can be expressed as

$$\frac{\sigma_1 - \sigma_3}{2} = \left\{ \begin{aligned} & [c_{\min}(b \sin^2 \alpha + \cos^2 \alpha) + 2\gamma_{\min}(a\sigma_r \sin^2 \alpha + \sigma_t \cos^2 \alpha + \tau_{tr} \sin 2\alpha)] \\ & \cdot [c_{\min}(\sin^2 \alpha + b \cos^2 \alpha) + 2\gamma_{\min}(a\sigma_r \cos^2 \alpha + \sigma_t \sin^2 \alpha - \tau_{tr} \sin 2\alpha)] \end{aligned} \right\}^{0.5} - \sin 2\alpha [\gamma_{\min} \sigma_r (a - 1) + c_{\min} (b - 1) / 2], \tag{9}$$

where a and b are both greater than 1; σ_r represents the stress along the bedding plane; σ_t refers to the stress perpendicular to the bedding plane; τ_{tr} is the shear stress on the bedding plane. σ_r , σ_t and τ_{tr} are calculated as follows:

$$\begin{aligned} \sigma_r &= \sigma_1 \sin^2 \alpha + \sigma_3 \cos^2 \alpha \\ \sigma_t &= \sigma_1 \cos^2 \alpha + \sigma_3 \sin^2 \alpha \\ \tau_{tr} &= \sin 2\alpha (\sigma_1 - \sigma_3) / 2. \end{aligned} \tag{10}$$

Accordingly, relevant parameters in Eq. (9) can be obtained by substituting relevant experimental data of shale into Eqs. (9) and (10) and through fitting, as shown in Table 1.

Jaeger. (1960) proposed the single weak surface (SWP) criterion in 1960, which is a typical discontinuous empirical criterion. Due to the different strengths of rock samples under bedding angles of 0° and 90° , the modified Jaeger criterion can be expressed as

$$\begin{cases} \tau_0 = c_0 + \sigma_n \tan \varphi_0 & (0^\circ \leq \alpha \leq \alpha_{\min}) \\ \tau_w = c_w + \sigma_w \tan \varphi_w & (\alpha_{\min} \leq \alpha \leq \alpha_{\max}) \\ \tau_{90} = c_{90} + \sigma_n \tan \varphi_{90} & (\alpha_{\max} \leq \alpha \leq 90^\circ) \end{cases}, \tag{11}$$

where c_w and φ_w are the cohesion and internal friction angle of the weak surface, respectively; c_0 , φ_0 , c_{90} , and φ_{90} represent the cohesion and internal friction angle of rock samples at bedding angles of 0° and 90° , respectively. If slip failure occurs on the weak bedding surface, the requirements should be as follows:

$$\sigma_1 = \sigma_3 + \frac{2c_w + 2\sigma_3 \tan \varphi_w}{(1 - \tan \varphi_w \cot \alpha) \sin 2\alpha}. \tag{12}$$

Similarly, relevant parameters in Eqs. (11) and (12) can be obtained by substituting relevant test data of shale into Eqs. (11) and (12) and through fitting, as shown in Table 1.

To construct a continuous empirical failure criterion more suitable for transversely isotropic rocks, Saeidi et al. (2013)

adjusted the rock failure criterion proposed by Rafiai (2011) as follows:

$$\sigma_1 = \left[\frac{1 + I(\sigma_3 / \sigma_{c\alpha})}{\eta + J(\sigma_3 / \sigma_{c\alpha})} \right] \sigma_{c\alpha} + \sigma_3, \tag{13}$$

where $\sigma_{c\alpha}$ is the uniaxial compressive strength of rock

under the bedding angle α ; I and J are constant parameters, which mainly depend on rock properties, and η means the strength reduction coefficient of rock. Relevant parameters in Eq. (13) can be obtained by substituting relevant test data of shale into Eq. (13) and through the fitting, as shown in Table 1.

To evaluate the accuracy and adaptability of five failure criteria, the fitting coefficient R^2 is set to evaluate the goodness of fit of each failure criterion, as follows (Yang et al. 2020):

$$R^2 = 1 - \frac{\sum_{i=1}^n (\sigma_i^e - \sigma_i^p)^2}{\sum_{i=1}^n (\sigma_i^e - A[\sigma^e])^2}, \tag{14}$$

where n is the total number of data points; σ_i^e and σ_i^p are the measured and predicted values at the i -th data point, respectively, and $A[\sigma^e]$ is the average of all measured values. The fitting coefficients (R^2) of different failure criteria are calculated by Eq. (14), as shown in Table 1.

Figures 16 and 17 show the strength envelope and fitting coefficient R^2 of shale samples in this experiment under different failure criteria, respectively. As can be seen from Figs. 16 and 17, the relationship between the maximum principal stress σ_1 and minimum principal stress σ_3 of Longmaxi Formation shale can be vividly described by the Mohr–Coulomb criterion, Hoek–Brown criterion, and other three anisotropic criteria.

However, compared with the linear strength criterion, the nonlinear strength criterion can better describe the experimental results of the Longmaxi Formation shale. According to the strength envelopes of the Mohr–Coulomb criterion and Hoek–Brown criterion (Fig. 16a), it seems the latter describes the experimental results better than the former. In addition, the fitting coefficient R^2 of the Hoek–Brown criterion is significantly larger than that of the Mohr–Coulomb criterion at different bedding angles (0° , 30° , 60° , 90°). The results of Fig. 16b show that, among three anisotropic criteria, the Saeidi criterion is more accurate in describing the experimental results

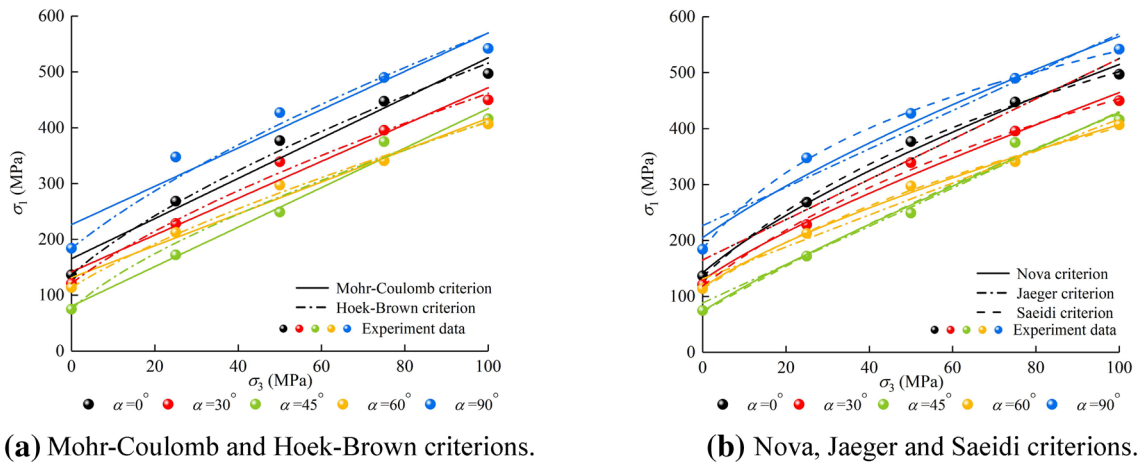


Fig. 16 Strength envelope of shale samples under different failure criteria

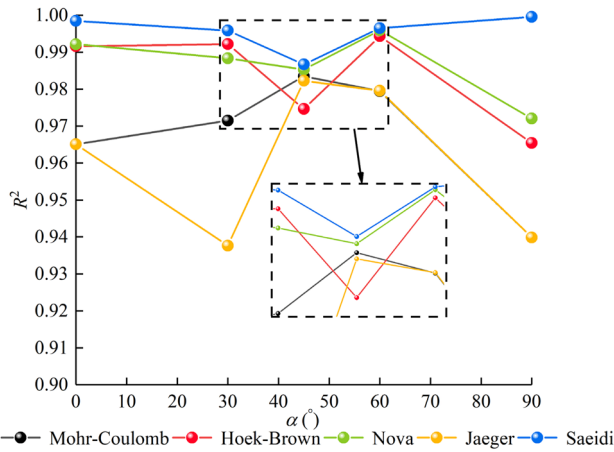


Fig. 17 Variation of fitting coefficient (R^2) with bedding angle α under different strength criteria

than the Nova criterion and Jaeger criterion. The fitting coefficient R^2 of the Saeidi criterion and Nova criterion under different bedding angles are significantly larger than that of the Jaeger criterion. Particularly, among the five strength criteria, the fitting coefficient R^2 of the Jaeger criterion is generally smaller, and it is even smaller than the Mohr–Coulomb criterion under bedding angles of 30° and 45° , which signifies Jaeger criterion is less qualified to describe the strength change and mechanical properties of shale, compared with the others. The main reason is that the shale strength predicted by the Jaeger criterion is always a constant value near bedding angles of 0° and 90° , and the mechanical property that shale strength changes with the bedding angle are ignored. Figure 18 lists the variation of predicted compressive strength with bedding angle under different strength criteria. It can be seen from Fig. 18 that the variation trend of predicted compressive

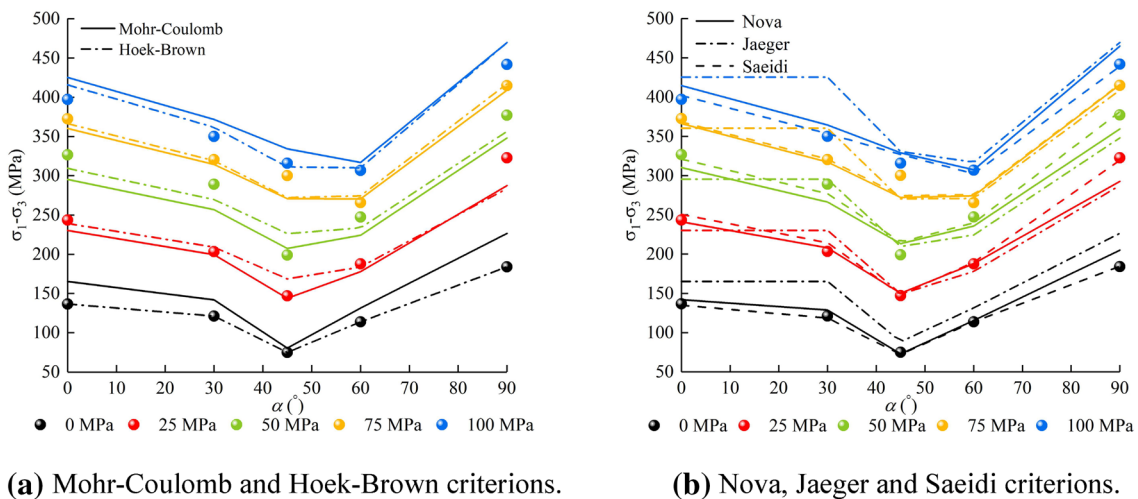


Fig. 18 Variation of compressive strength ($\sigma_1 - \sigma_3$) with bedding angle α under different strength criteria

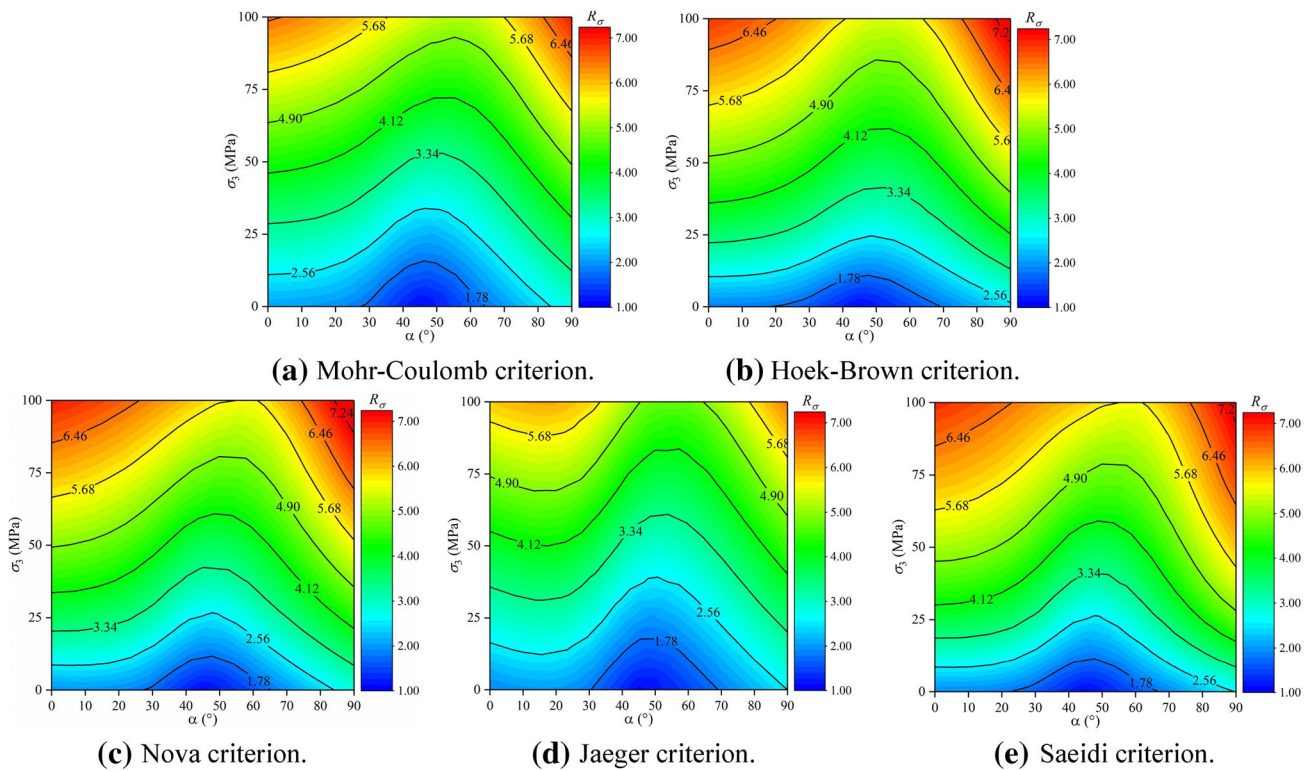


Fig. 19 Distribution of relative strength R_σ for predicting strength under different strength criterions

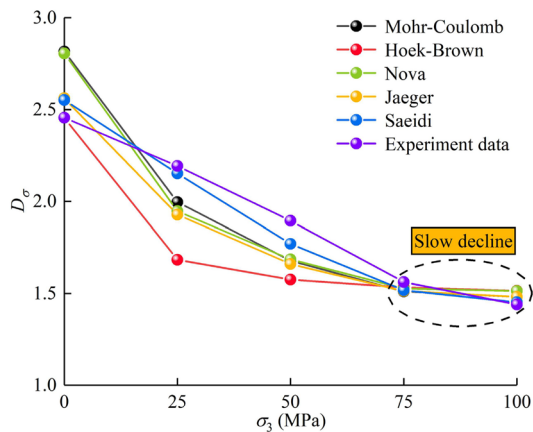


Fig. 20 Degree of anisotropy D_σ of predicted compressive strength under different strength criterions

strength with the bedding angle under five strength criteria is consistent with that of compressive strength in the experiment. Five strength criteria can describe the unique behavior that “dangerous bedding angle” increases from 45° to 60° in the process of confining pressure increasing from low to high.

To further analyze the adaptability and accuracy of five strength criteria, the predicted values under five strength criteria are substituted into Eqs. (2) and (3) to obtain

the relative strength R_σ and anisotropy of compressive strength D_σ under different strength criteria, as shown in Figs. 19 and 20. Compared with the relative strength R_σ obtained from the experiment of Longmaxi Formation shale (Fig. 15a), the relative strength R_σ under five strength criteria has changed, but changing trends with bedding angle and confining pressure are roughly consistent. Under the same bedding angle, the relative strength R_σ under different strength criteria increases as confining pressure rises. Under the same confining pressure, the relative strength R_σ under the five strength criteria also varies in a trend of “decrease first, then increase” when the bedding angle increases from 0° to 90° . Following the variation of D_σ with confining pressure under five strength criteria (Fig. 20), the anisotropy degree of predicted compressive strength declines with the increase of confining pressure, and under high confining pressures ($\sigma_3 = 75$ MPa, 100 MPa), the weakening effect of confining pressure on anisotropy degree also declines. This shows that these five strength criteria can effectively reveal the effect of confining pressure on the anisotropy of Longmaxi Formation shale, as shown in Fig. 20.

Interestingly, it can be seen from Fig. 20 that under confining pressures of 0 MPa, 100 MPa, five strength criteria will amplify the anisotropy degree of compressive strength, while under 25 MPa, 50 MPa, and 75 MPa, these five

strength criteria will reduce the anisotropy degree of compressive strength.

4.2 AE Characteristics Analysis of Longmaxi Formation Shale

Acoustic emission (AE) is a technique widely used to study the characteristics of rock deformation and failure. The characteristics of AE activities are tightly related to the closure and propagation of cracks in rock (Byerlee 1978; Lockner 1993; Lyu et al. 2021b). For transversely isotropic rocks, such as shale, the closure and propagation of internal cracks are not only related to confining pressure in the triaxial compression test but also influenced by anisotropy so that cracks closure and propagation are far from the same under different bedding angles.

To investigate the cracks closure and propagation in Longmaxi Formation shale under different confining pressures and bedding angles, the AE response characteristics of shale in triaxial compression test are analyzed (taking shale with bedding angle of 30° and 25 MPa confining pressure

as examples, respectively). The variation patterns of stress, AE ringing counts (number of ringing counts when the AE signal exceeds the threshold value per unit time), cumulative ring counts (total number of ringing counts when the AE signal exceeds the threshold value during the test), and cumulative energy (total count of energy during the test) of the Longmaxi Formation shale under different confining pressures and bedding angles over time are drawn in Figs. 21 and 22. In the initial loading stage (macroscopic near-linear elastic deformation stage I), affected by the compression, a small number of AE events with low AE ringing counts and energy occurred, and cumulative ring counts and cumulative energy begin to increase, which is different from the previous statement on the macro-mechanical performance of shale. The main reason is that although the larger microcracks and weak bedding planes have been highly compacted and closed before the application of axial load, the deformation of shale is near-linear elastic deformation in the macroscopic view, a small number of microcracks inside the shale are not compressed. These microcracks are compacted tightly under the axial stress and confining pressure

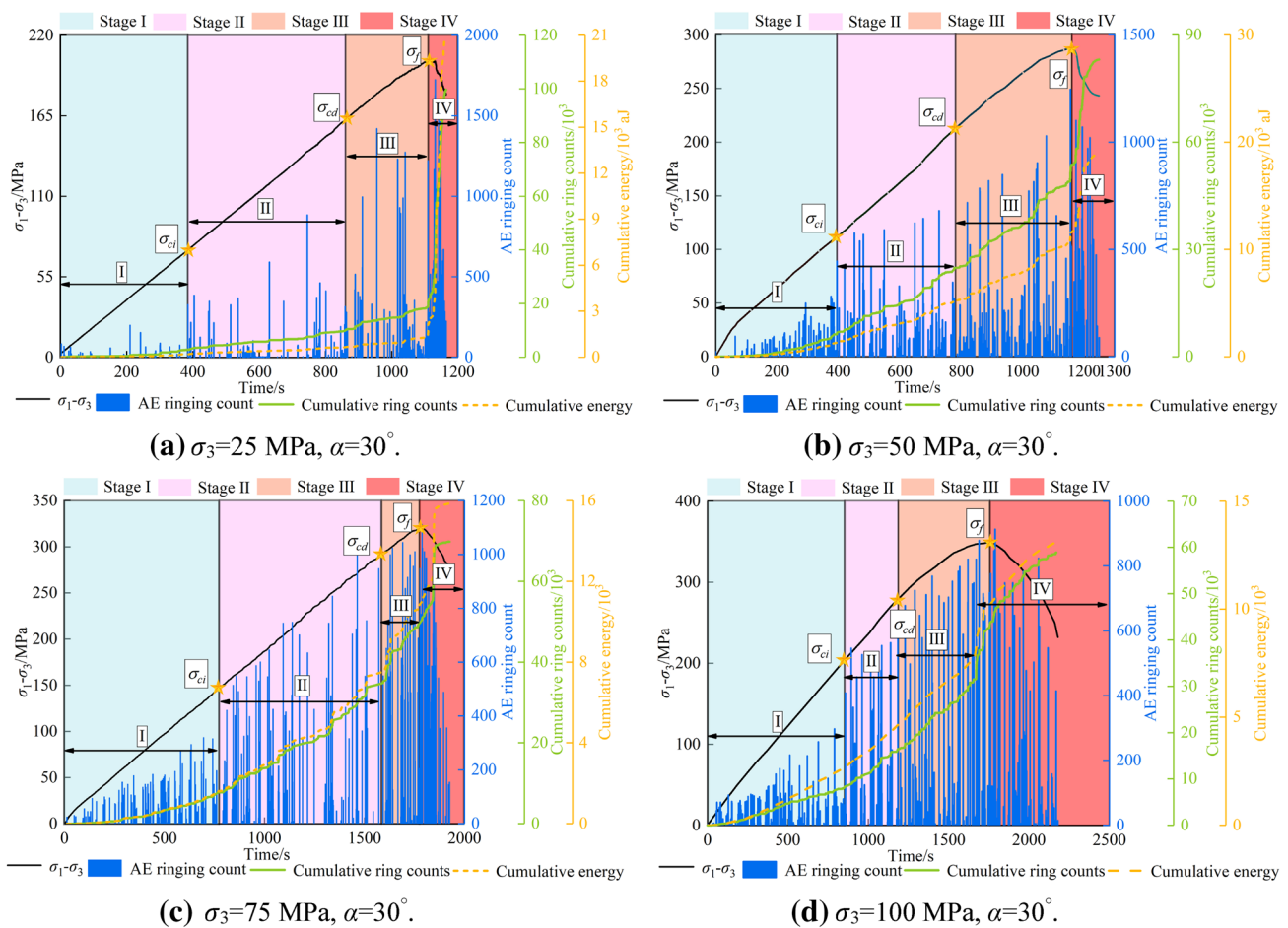


Fig. 21 AE characteristic curves of shale under different confining pressures

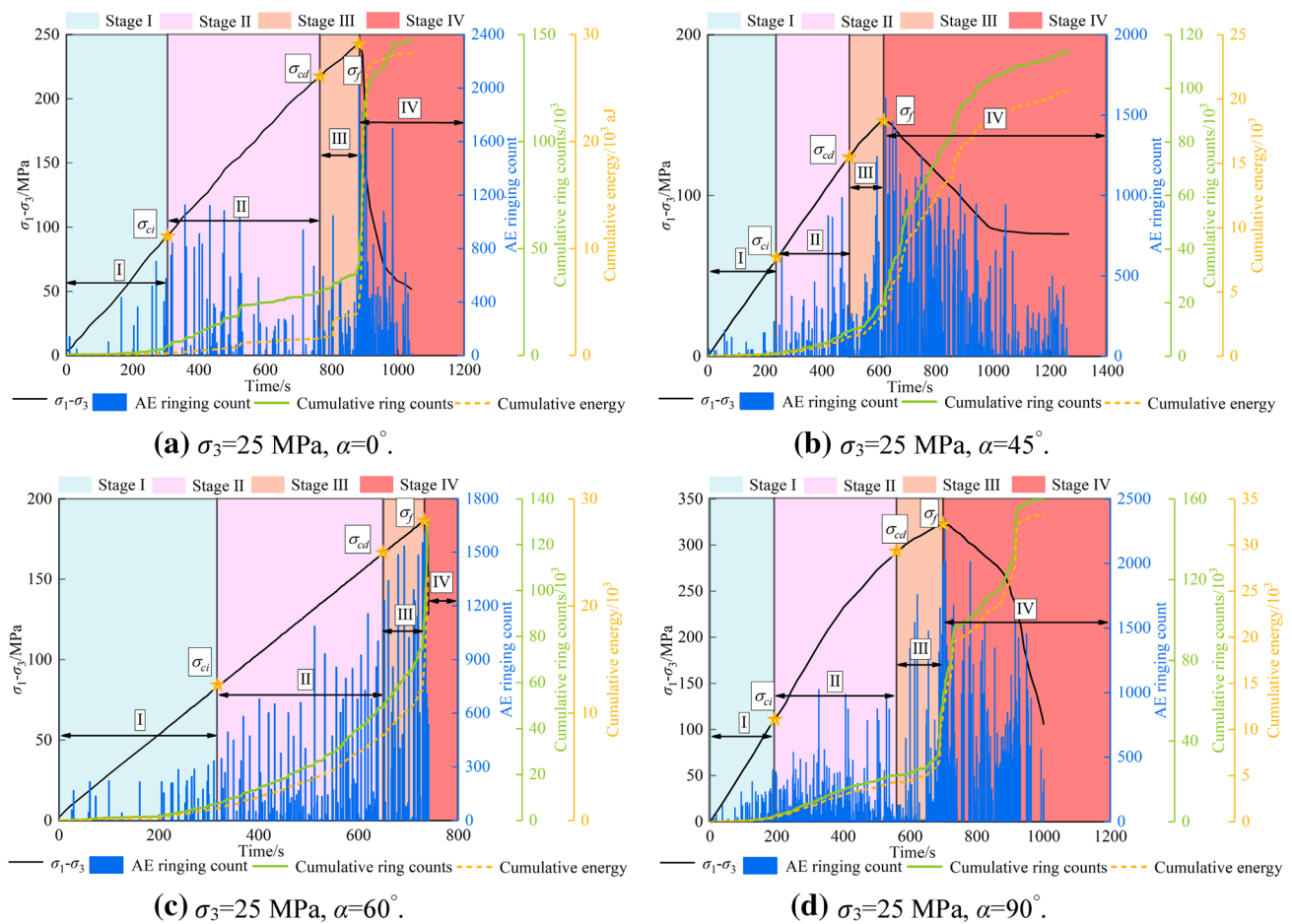


Fig. 22 AE characteristic curves of shale under different bedding angles

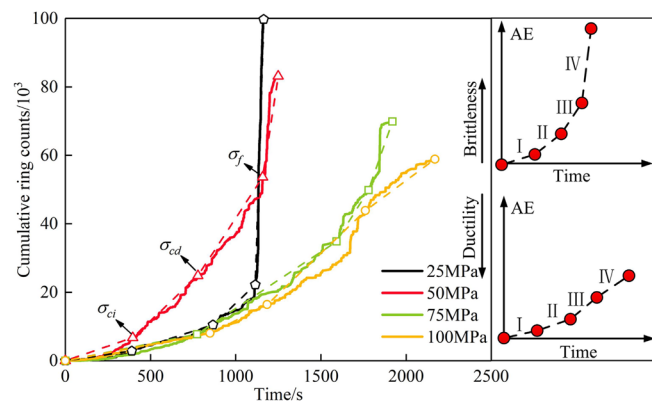
to radiate elastic waves, resulting in AE signals with a small number of AE ringing counts in the initial loading stage. With the continuous application of axial load, the microcracks in the shale begin to appear, and propagate and connect; the cohesion between bedding and matrix becomes weakened, and the bedding is activated and slipped, resulting in the increase of AE events, the cumulative ring counts and cumulative energy rise slowly with time, and the increase rate accelerates gradually. When reaching the peak stress σ_p , the AE ringing counts are the highest. Specifically, near the peak stress σ_p , the AE ringing counts of shale samples with 30° bedding angle under 25 MPa and 75 MPa confining pressure reach the maximum values of 1724 times/s and 1111 times/s, respectively. At this time, shale samples are also close to failure. After the peak stress σ_p , shale samples enter the bedding severely slips and post-peak failure stage IV, and the AE ringing counts begin to decrease until shale samples fail eventually.

As a whole, the variation of cumulative ring counts and cumulative energy with time is roughly the same. The AE ringing counts of shale are in a changing pattern of “first

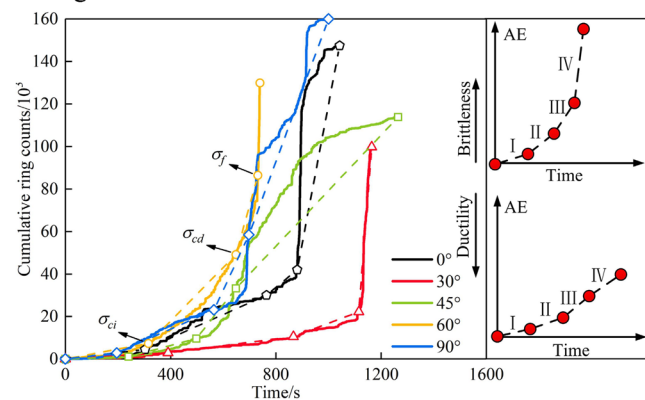
increase and then decrease” over time, and they are lower in the entire macroscopic near-linear elastic deformation stage I and end of the bedding severely slips and post-peak failure stage IV.

Moreover, it can be seen from Figs. 21 and 22 that the AE response characteristics of the Longmaxi Formation shale are dramatically impacted by confining pressure and bedding angle, and the AE evolution displays different characteristics under different confining pressures and bedding angles. When $\sigma_3 = 25$ MPa, $\alpha = 30^\circ$ and $\sigma_3 = 25$ MPa, $\alpha = 0^\circ$ (Figs. 21a and 22a), the AE events appear intermittently, and AE ringing counts are all larger, which decrease rapidly and then remain at a small value in stage IV. The cumulative ring counts and cumulative energy increase slowly with time before peak stress σ_p , but rise rapidly to the maximum value in stage IV. According to the method of identifying AE types proposed by Zhang et al. (2018), the AE evolution of shale shows characteristics of brittle failure under $\sigma_3 = 25$ MPa, $\alpha = 30^\circ$ and $\sigma_3 = 25$ MPa, $\alpha = 0^\circ$, as shown in Fig. 23. However, under the condition of $\sigma_3 = 25$ MPa, $\alpha = 45^\circ$ and $\sigma_3 = 100$ MPa, $\alpha = 30^\circ$ (Figs. 21d and 22b), AE

Fig. 23 Cumulative ring counts–time curves of shale under different confining pressures and bedding angles



(a) Cumulative ring counts–time curves of shale under different confining pressures.



(b) Cumulative ring counts–time curves of shale under different bedding angles.

events occur frequently, but the peak value of AE ringing counts is small. During the whole process of the experiment, the cumulative ring counts and cumulative energy continue to grow slowly, and the growth rate is significantly smaller than that at $\sigma_3 = 25$ MPa, $\alpha = 30^\circ$, and $\sigma_3 = 25$ MPa, $\alpha = 0^\circ$ (Fig. 23), which indicates that the brittle failure characteristics of AE evolution are weakened and show the characteristics of plastic failure.

In Fig. 23a, with confining pressure increasing, the increase rate of cumulative ring counts declines gradually, and the AE response characteristic of brittle failure gradually weakens and displays plastic failure. According to Fig. 23b, the cumulative ring counts of shale at 25 MPa confining pressure in stage IV show a higher increase rate with time, but the AE event trigger rate and AE ringing counts still change differently with the bedding angles, which again confirms that the brittleness of shale is also anisotropic (Fig. 22). Under confining pressure of 25 MPa, AE events of shale at the 45° bedding angle are more densely distributed than that at other bedding angles. In addition, the peak value of AE ringing counts is the smallest, cumulative ring counts increase the slowest over time, and plastic failure characteristics are found in AE evolution. In a word, the AE evolution of Longmaxi Formation shale can qualitatively characterize its brittleness, which is more consistent with the brittleness

evaluation results based on the stress–strain curve form. When the distribution of AE events is much denser, and the peak value of AE ringing counts is smaller, the rise of cumulative ring counts and cumulative energy is smoother over time, and the lower the brittleness of Longmaxi Formation shale. In return, the higher the brittleness of Longmaxi formation shale, the lower the triggering rate of AE events, the higher the peak value of AE ringing count of a single event, the abrupt change of cumulative ring counts and cumulative energy will occur in stage IV and rise sharply with time.

In the triaxial compression test, shale will undergo fractures with different scales at different loading stages, and the peak frequencies of AE signals will also change. Figures 24 and 25 introduce the distribution of peak frequencies (frequency corresponding to the maximum energy spectrum point) of Longmaxi Formation shale under different confining pressures and bedding angles, respectively. The peak frequencies of Longmaxi Formation shale are in zonal distribution, mainly distributed in four frequency bands of 0–50 kHz, 50–100 kHz, 100–150 kHz, and 150–350 kHz, of which 0–50 kHz frequency band accounts for the highest proportion of peak frequencies, about 50–65%. It shows from Figs. 24 and 25 that when shale enters stage IV from stage III, fewer high-frequency signals occur and low-frequency signal increases clearly. The main reason is that

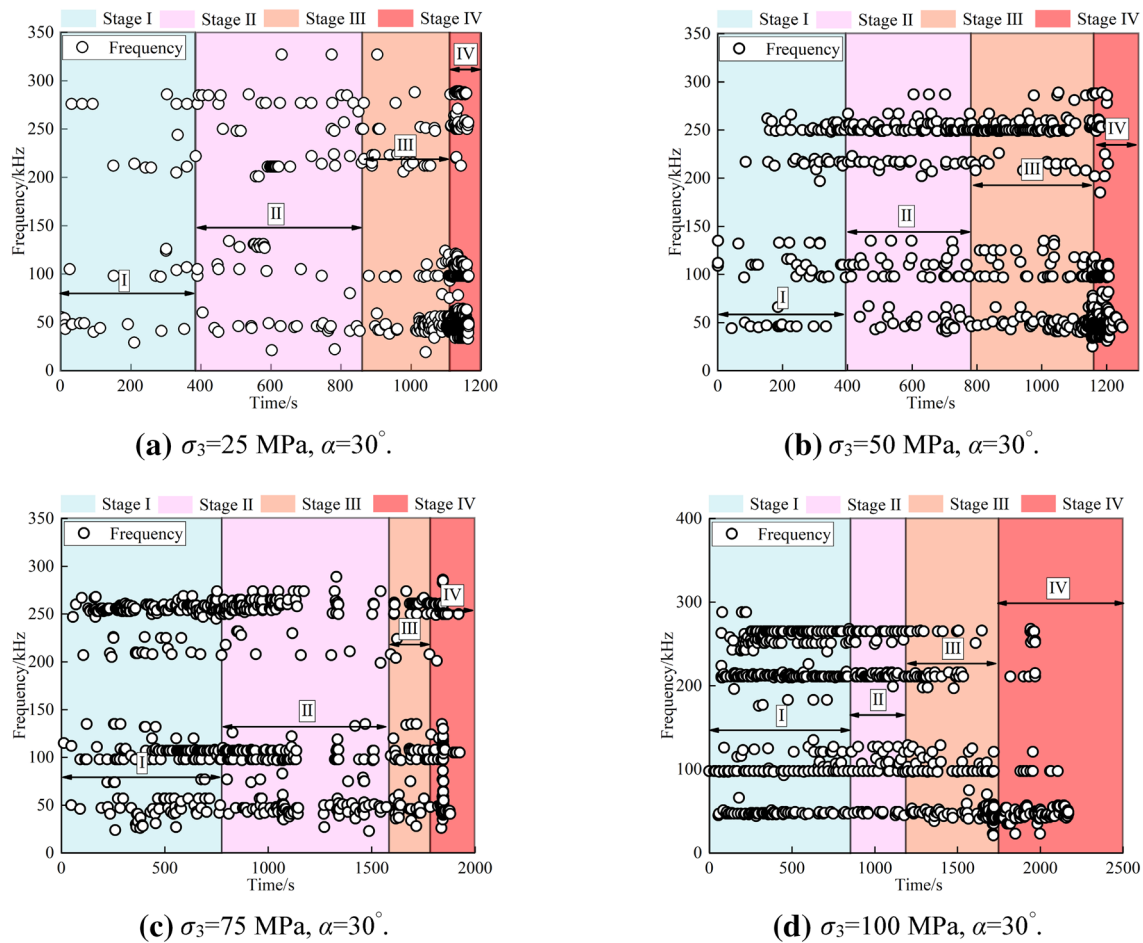


Fig. 24 Peak frequency of shale under different confining pressures

the stress drops sharply in stage IV, and due to the friction of macroscopic through fractures in the shale, the bedding plane slips violently, enlarging the rupture scale dramatically. Eventually, lots of low-frequency signals occur. This is consistent with the findings of Ohnaka and Mogi (1982) on the correlation between rupture scale and peak frequencies.

To clarify the distribution of peak frequencies in different stages, the distribution ratios of peak frequencies in four stages under different confining pressures and bedding angles are collected, as shown in Figs. 26 and 27. The proportion of peak frequencies is not the same in different stages. Shale experiences microscopic fractures in stage I and stage II, and the rupture scale is small, such as coupling of mineral particles in shale matrix and bedding plane, or fractures along and within crystal interface (crystal interface dislocation, intergranular failure, transgranular failure, etc.). Thus, the high-frequency signals (150–350 kHz) always occupy the highest proportion in stage I and stage II regardless of the variation of confining pressure and bedding angle. Nevertheless, the proportion of low-frequency signals (0–50 kHz) is the highest in stage III and stage IV,

because microcracks in the shale have penetrated each other, and the bedding plane slips with a large rupture scale. It is worth noting that from the distribution of peak frequencies in different stages (Figs. 26 and 27), the distribution does not seem to show obvious regular changes with confining pressure and bedding angle. Therefore, the total proportion of peak frequencies under different confining pressures and bedding angles is counted, as shown in Fig. 28. Due to the binding effect of confining pressure on shale sample, the rupture scale of shale gradually decreases in the process of confining pressure increases; the total proportion of low-frequency signals (0–50 kHz) falls, while that of high-frequency signals (150–350 kHz) rises (Fig. 28a). In Fig. 28b, under confining pressure of 25 MPa and bedding angle of 45°, the total proportion of low-frequency signals (0–50 kHz) is the highest, indicating that shale has a larger rupture scale under such conditions. In addition, it is found that the confining pressure affects the total proportion of peak frequency more greatly than bedding angle.

In the research of seismology, the frequency of seismic signal is tightly related to the focal dimension, and

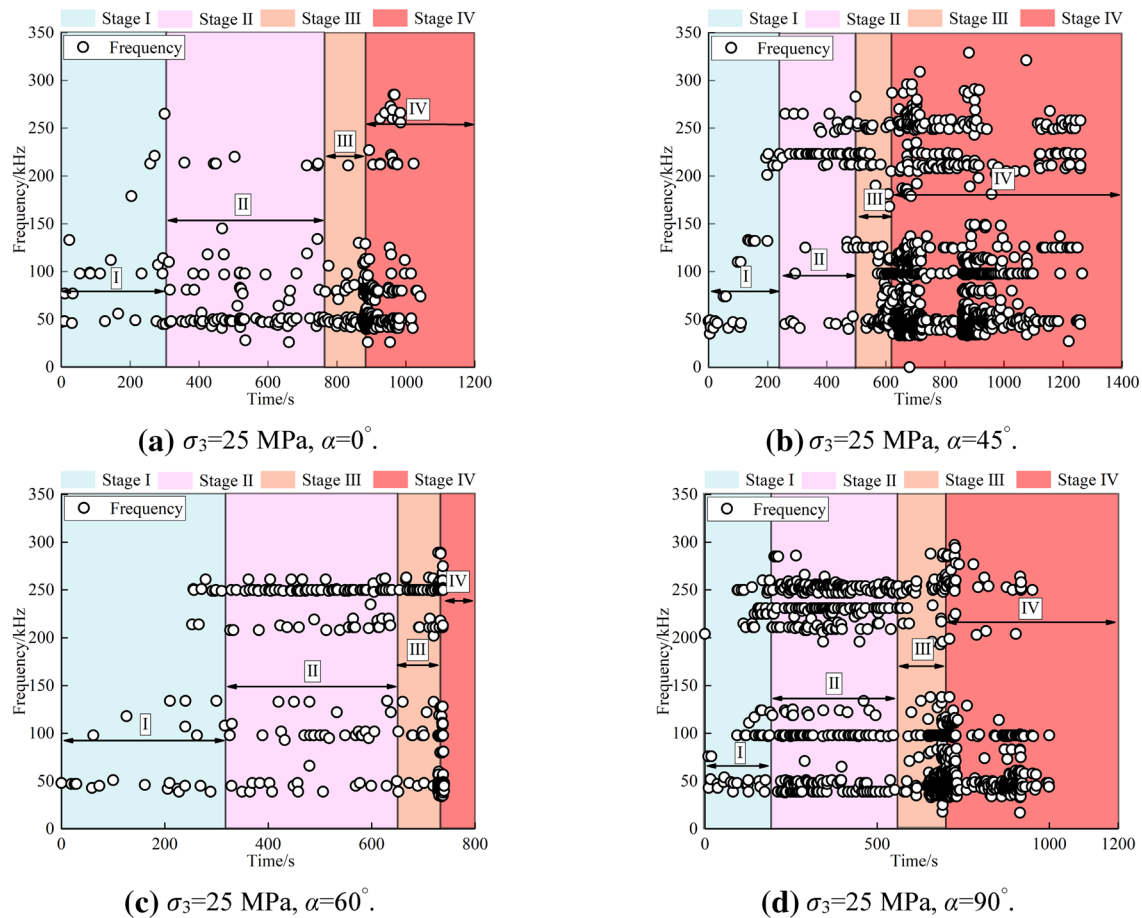


Fig. 25 Peak frequency of shale under different bedding angles

the focal dimensions of different frequency signals can be evaluated by the method of focal dimension-frequency scaling (Benson et al. 2010; Zurich et al. 2007). Similarly, it can be seen from the above analysis that the rupture scale of shale is well correlated to peak frequency at different loading stages. Benson et al. (2010) proposed the relationship between the frequency and focal dimension when earthquakes were simulated by laboratory AE tests, as shown in the following:

$$S_L \times f_L = S_e \times f_e, \quad (15)$$

where S_L is the rupture scale in laboratory test; f_L means the frequency in laboratory test; S_e refers to the focal dimension of the earthquake; f_e represents the focal frequency of the earthquake.

When the natural earthquake scale is 0.2–1 km, the focal frequency shall be distributed in 1–2 Hz (Benson et al. 2010). Since both focal dimension and frequency of natural earthquakes are determined, it can be seen from Eq. (15) that the larger the rupture scale of laboratory test, the smaller the corresponding frequency. When the peak

frequency in laboratory test is 100–200 kHz, the rupture scale should be between 2 and 10 mm theoretically, which is millimeter level; when the peak frequency is less than 100 kHz, the rupture scale should be greater than 10 mm, at a centimeter level. In summary, based on the above statistical results, due to the existence of bedding planes, the internal structure of shale will be damaged in the triaxial compression test, and the rupture scale is at the centimeter level. Both confining pressure and bedding angle affect the failure scale of shale. Specifically, as confining pressure increases from 25 to 100 MPa (Fig. 28a), the rupture scale of shale will change from centimeter level to millimeter level. Under low confining pressure (25 MPa), shale with a bedding angle of 45° undergoes slip failure due to the influence of bedding planes, and the rupture scale is the largest. When shale transitions from the bedding activation and stable microcracks propagation stage II to bedding initiation slip and unstable microcracks propagation stage III, the rupture scale will also increase.

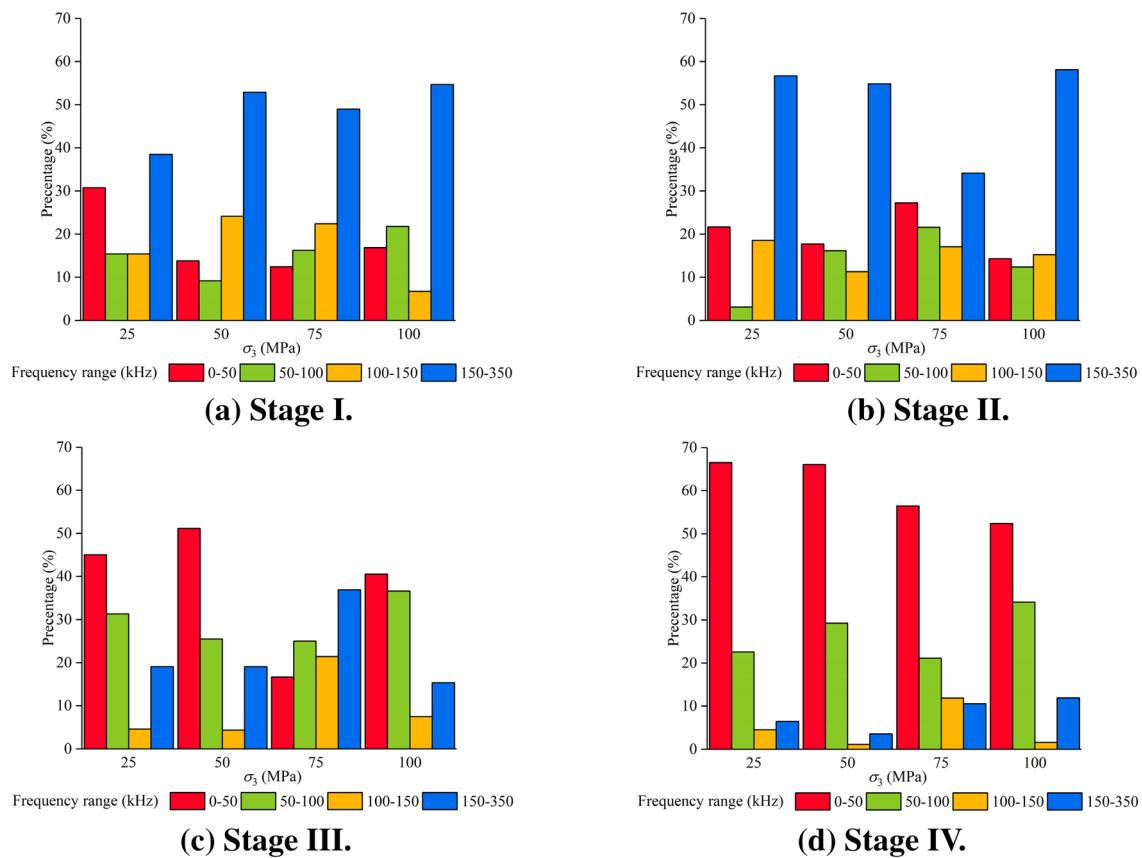


Fig. 26 Distribution of peak frequency bands under different confining pressures

4.3 Failure Modes Analysis of Longmaxi Formation Shale

Figure 29 shows the failure modes of Longmaxi formation shale with different bedding angles under various confining pressures. The failure modes of Longmaxi Formation shale seem complex and irregular. However, from the changing trend of failure modes with confining pressure and bedding angle, the failure modes show a significant confining pressure effect and bedding effect. Under low confining pressures (0 MPa, 25 MPa, and 50 MPa), shale samples with bedding angles of 0° and 30° produce non-penetrating vertical cracks and multiple fractures along the bedding direction, forming a complex fracture network. For shale samples with bedding angles of 45° and 60° , because the bedding planes with inclination angles of 45° and 60° are easily activated under the critical stress, shale samples with bedding angles of 45° and 60° will produce single or multiple oblique fractures extending along bedding plane under low confining pressure, mainly dominated by slip failure along the weak bedding plane. The shale samples with a bedding angle of 90° show splitting failure characteristics under low confining pressure, mainly dominated by bedding fractures through shale. As

confining pressure increases from low (0 MPa, 25 MPa, 50 MPa) to high (75 MPa, 100 MPa), under the confining pressure effect, the number of cracks along the bedding planes of shale samples under different bedding angles is reduced, and instead, complex and disordered cracks network gradually transforms into a single shear crack. This is consistent with the previous conclusion that “increasing confining pressure will reduce the anisotropy of shale”. When shale gas is exploited by hydrofracturing technology under high crustal stress, attention should also be paid to the connectivity and effectiveness of fracture network.

Summarizing failure behavior and modes of Longmaxi formation shale (Fig. 30), this study found that under low confining pressures (0 MPa, 25 MPa, 50 MPa), there are mainly four failure modes such as conjugate shear failure, splitting through bedding plane, splitting along bedding plane, and shear along bedding plane. Under high confining pressures (75 MPa, 100 MPa), there are mainly two failure modes: shear along bedding plane and shear through bedding plane. Five failure modes not only change with confining pressure but also are tightly related to bedding angle. Table 2 shows failure modes of Longmaxi Formation shale under different confining pressures and bedding angles. Five failure modes are analyzed as follows:

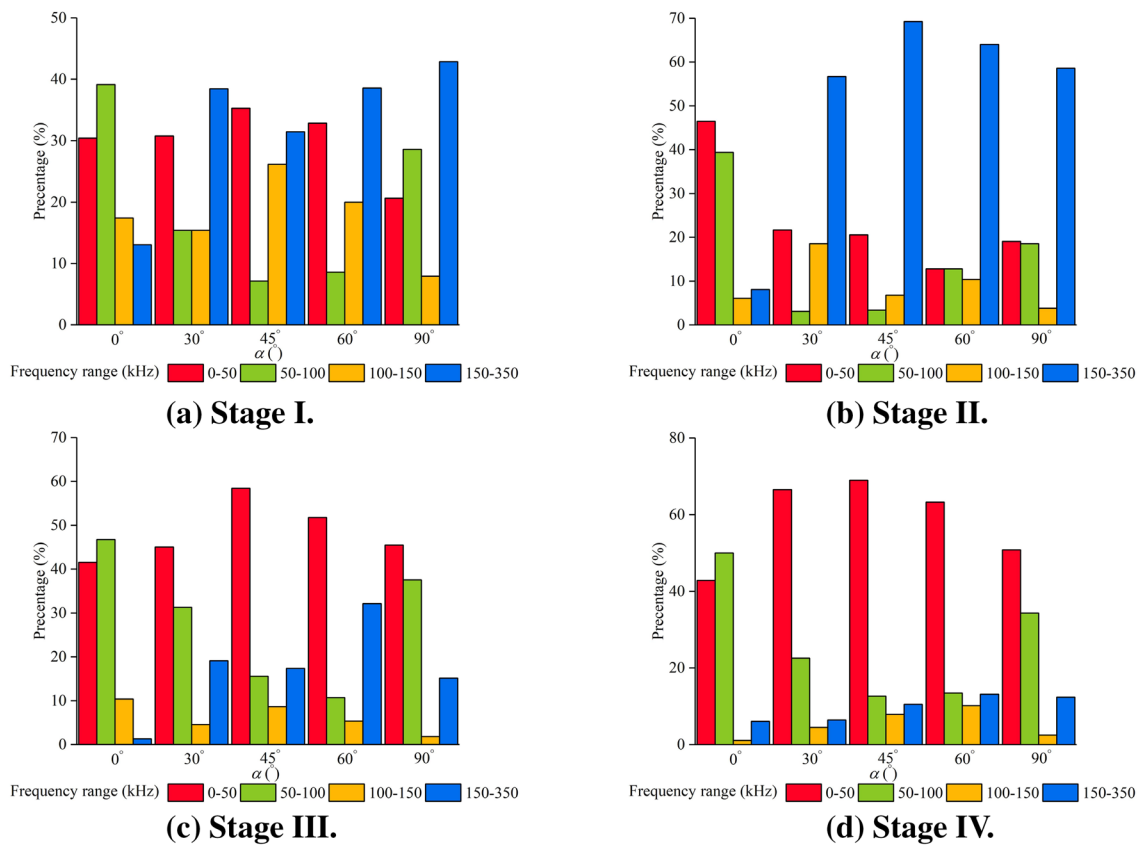


Fig. 27 Distribution of peak frequency bands under different bedding angles

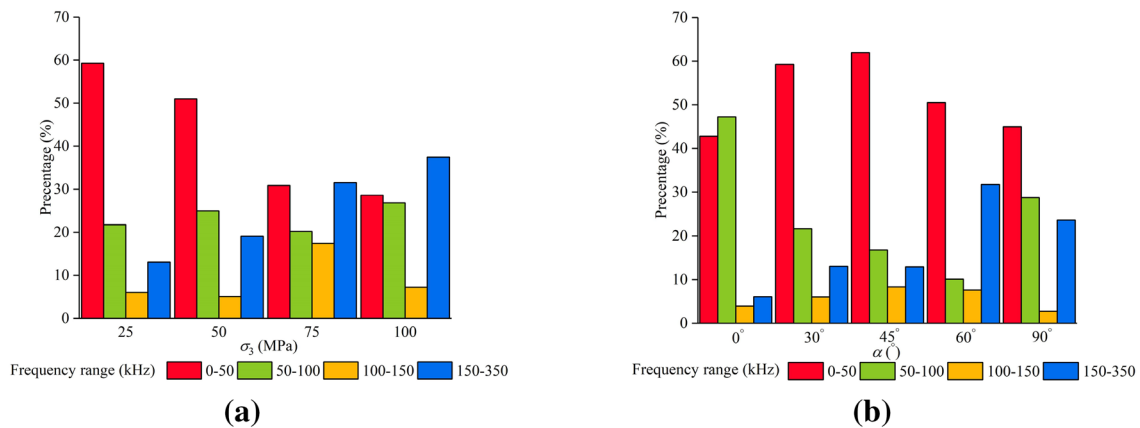


Fig. 28 Total proportion of the peak frequency bands under different **a** confining pressures and **b** bedding angles

1. Conjugate shear failure (Co-Sh): Conjugate shear occurs mainly in shale samples with bedding angles (30°, 45°, 60°) under low confining pressures (0 MPa, 25 MPa, 50 MPa). Under low confining pressure, shale samples are subject to small lateral restraint and larger axial stress. Due to the influence of end effect, after shale samples slip along the bedding plane on one side of the

end, the axial stress is fully concentrated on the other side of the end, causing shear cracks on the other side. Eventually, cracks on both sides form a V-shaped conjugated major fracture.

2. Splitting through bedding plane (Sp-Th): This mode occurs in shale samples with the bedding angle below 45° under low confining pressure. Because the angle

Fig. 29 Failure modes of Long-maxi Formation shale



between the bedding plane below the bedding angle of 45° and axial stress is larger, and the lateral restraint is small, the shale is induced to produce tensile fractures parallel to the direction of maximum principal stress, accompanied by slip fractures and related secondary cracks along the bedding direction.

3. Splitting along bedding plane (Sp-A1): Under low confining pressure, when the bedding angle of shale increases to 90° , the maximum principal stress is consistent with the direction of bedding plane. Due to the weak binding effect of confining pressure, the bedding planes are stretched and opened under axial stress, which

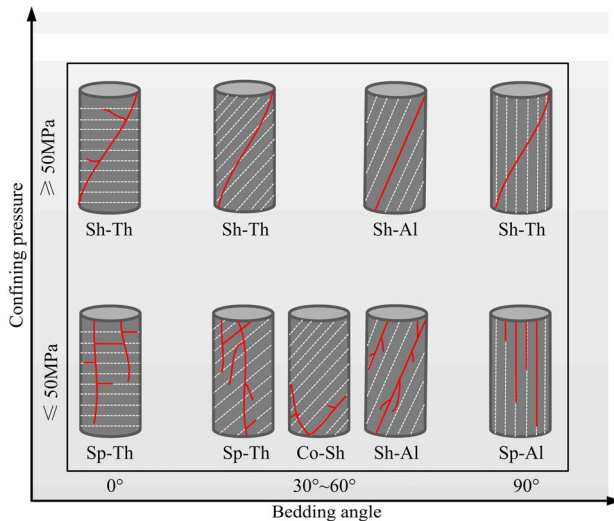


Fig. 30 Main failure modes of shale under different confining pressures and bedding angles

Table 2 Failure modes of Longmaxi Formation shale under different confining pressures and bedding angles

	0 MPa	25 MPa	50 MPa	75 MPa	100 MPa
0°	Sp-Th	Sp-Th	Sh-Th	Sh-Th	Sh-Th
30°	Sp-Th	Sp-Th	Co-Sh	Co-Sh, Sh-Al	Sp-Th, Sh-Al
45°	Co-Sh, Sp-Th	Co-Sh, Sp-Th	Sh-Al	Sh-Al	Sh-Al
60°	Sp-Th, Sh-Al	Sh-Al	Co-Sh	Sh-Al	Sh-Al
90°	Sp-Al	Sp-Al	Sp-Al	Sh-Th	Sh-Th

eventually leads to the formation of vertical multiple-splitting failure.

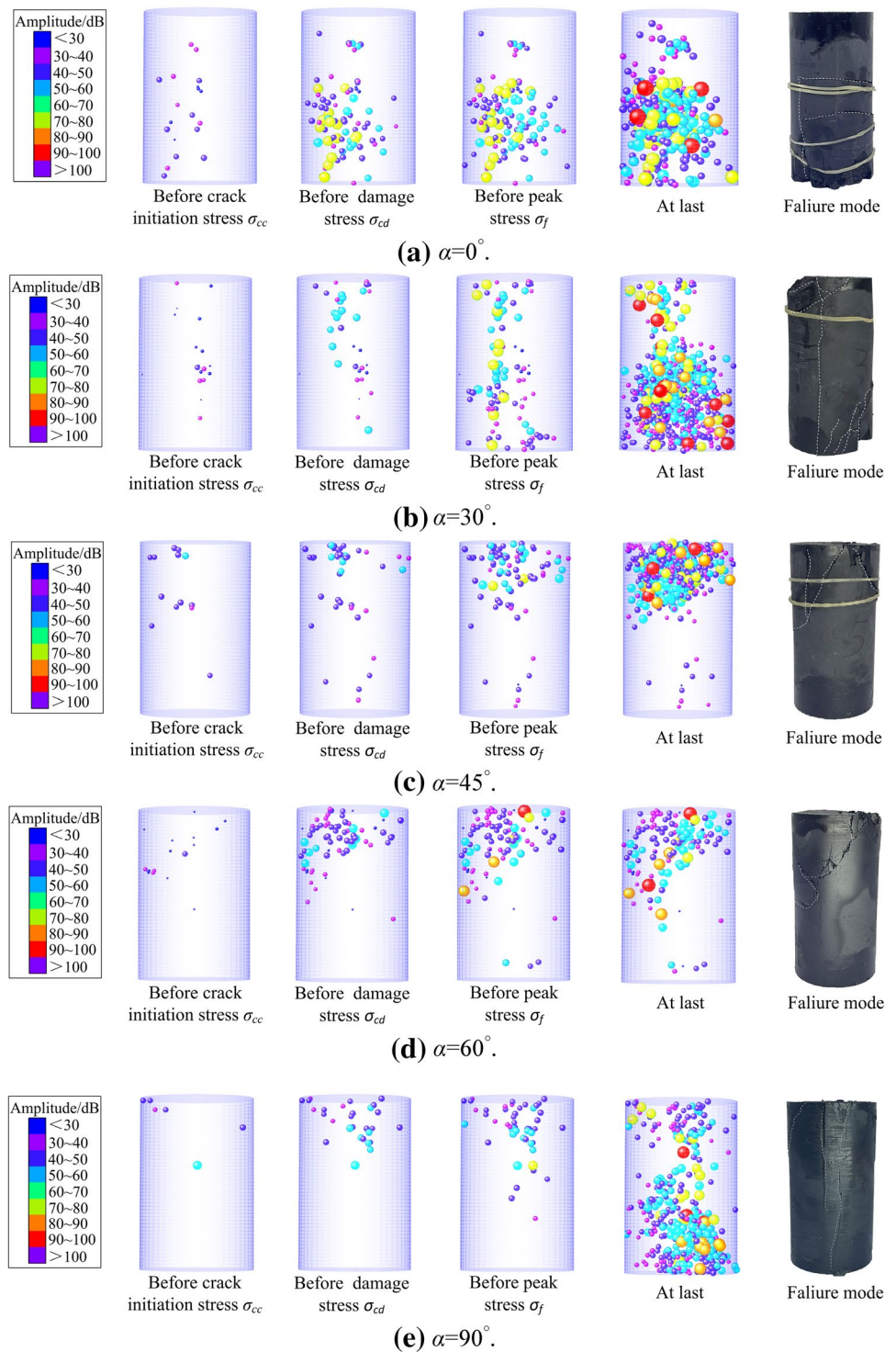
4. Shear along bedding plane (Sh-Al): The Sh-Al failure mode is caused mainly by shear slip failure of shale samples with larger bedding angles (45°, 60°) along the bedding plane. The main reason is that the bedding plane with a larger angle is easier to lose the cohesive force under the axial load than the shale matrix, and finally, single or multiple macro shear planes are formed along the bedding plane direction.
5. Shear through bedding plane (Sh-Th). Under high confining pressure, the binding effect of confining pressure inhibits the brittleness and bedding effect of Longmaxi Formation shale, so that the shale will not produce more microcracks along the direction of bedding plane. Eventually, only the macroscopic shear planes through the bedding planes are formed, such as shale samples with bedding angles of 45° and 60° under 100 MPa.

4.4 Discussion on the Relationship Between AE Characteristics, Brittleness, and Failure Modes of Shale

AE response characteristics of Longmaxi Formation shale can not only qualitatively characterize the brittleness (Sect. 4.2), but also are related to failure modes (Zhao et al. 2022). To reveal the relationship between AE response characteristics and failure modes, this study calibrated and analyzed the AE source location, as shown in Fig. 31 (taking shale with different bedding angles under 25 MPa confining pressure as an example). Figure 31 describes the amplitude distribution of the AE source in different loading stages. It can be seen that the amplitude evolution reflects the development of AE events in real time. Before the cracks initiation stress σ_{cc} , since the shale is in stage I (macroscopic near-linear elastic) at this time, AE events are all randomly and discretely distributed, and most of the amplitudes are below 50 dB. When Longmaxi Formation shale enters stage II (bedding activation and stable microcrack propagation), the amplitude gradually increases (the amplitude is greater than 50 dB), and AE events grow and are aggregated distribution. This means that the bedding inside shale samples is activated and cracked, and the microcracks begin to penetrate. At peak stress σ_f , the bedding begins to slip, and the growing range and rate of microcracks increase. Meanwhile, more AE events with amplitude greater than 70 dB increase and are clustered. The main reason is that the bedding and matrix of shale samples at peak stress σ_f debond and start to slip, and strain energy stored by mutual bonding of shale particles in the matrix is relatively high, forcing shale samples to release more energy during bedding slip and matrix fracture process. With the continuous loading of axial stress, shale enters stage IV (bedding severely slips and post-peak failure), and AE events with amplitude greater than 90 dB begin to appear. According to Fig. 31, the distribution of AE events in the final is tightly related to failure modes. The distribution of AE events can reflect failure modes of shale samples, and AE events with higher amplitudes are concentrated and distributed in the macro-fracture zone and near the bedding slip position.

From the above analysis, it can be seen that the AE response characteristics of shale can not only qualitatively characterize the brittleness but also directly display failure modes of shale. At present, the brittleness index is widely used to quantitatively analyze the brittleness of shale. Table 3 lists common BIs about the proportion of shale mineral composition and stress-strain curve. In accordance with the mineral composition proportion of Longmaxi Formation shale in Sect. 2.2, it obtains $BI_1 = 0.655$, $BI_2 = 0.575$, and $BI_3 = 0.904$, respectively, all greater than 0.5. Therefore, shale samples selected in this experiment

Fig. 31 Main failure modes of shale under different confining pressures and bedding angles



are relatively brittle from the perspective of mineral composition. The fact is that the brittleness is not only related to mineral composition, and may change under different stress environments. Therefore, it is particularly significant to analyze the brittleness based on the stress–strain curve. By referring to the deformation and strength parameters

of shale in Sect. 4.1, this study calculated $BI_4 \sim BI_8$ under different confining pressures and bedding angles, respectively. To evaluate the relative degree of brittleness between $BI_4 \sim BI_8$, Eqs. (16) and (17) are used to normalize $BI_4 \sim BI_8$, respectively (Zhai et al. 2021a). The normalized brittleness indexes under different confining pressures and bedding angles are shown in Figs. 32 and 33

Table 3 Common BIs about the proportion of shale mineral composition and stress–strain curve

Classification	Analytical formula	References	Abbreviations
Mineral composition	$BI_1 = \frac{W_q + W_c}{W_{tot}}$	Rickman et al. (2008)	W_q = Weight percentage of quartz; W_c = Weight percentage of calcite; W_d = Weight percentage of dolomite; W_{cl} = Weight percentage of clay; W_{qmf} = Weight percentage of quartz, mica and feldspar; W_{tot} = Total mineral weight
	$BI_2 = \frac{W_{cl}}{W_q + W_{cl} + W_c}$	Jarvie et al. (2007)	
	$BI_3 = \frac{W_{qmf} + W_c + W_d}{W_{tot}}$	Jin et al. (2015)	
Stress–strain curve	$BI_4 = \frac{\varepsilon_e}{\varepsilon_f}$	Hucka and Das (1974a)	ε_e = Elastic strain; ε_f = Peak strain; ε_r = Residual strain; σ_f = Peak Stress; σ_r = Residual Stress; M = post-peak modulus
	$BI_5 = \frac{\varepsilon_f}{\varepsilon_r}$	Hajiabdolmajid and Kaiser (2003)	
	$BI_6 = \frac{\varepsilon_f - \varepsilon_r}{\varepsilon_f}$	Martin (1996)	
	$BI_7 = \frac{\sigma_f - \sigma_r}{\sigma_f}$	Bishop (1967)	
	$BI_8 = \frac{\sigma_f - \sigma_r}{\sigma_f} \lg M $	Yang et al. (2020)	

$$BI_{\Delta 1} = \frac{BI_x - BI_{\min}}{BI_{\max} - BI_{\min}}, \quad (16)$$

$$BI_{\Delta 2} = \frac{BI_x - BI_{\max}}{BI_{\min} - BI_{\max}}, \quad (17)$$

where $BI_{\Delta 1}$ stands for the normalization of indexes positively related to brittleness; $BI_{\Delta 2}$ represents the normalization of indexes negatively related to brittleness; BI_x means $BI_4 \sim BI_8$; BI_{\max} refers to the maximum brittleness index under the same confining pressure or bedding angle; BI_{\min} is the minimum brittleness index under the same confining pressure or bedding angle.

Figure 32 describes the variation trend of normalized brittleness indexes with confining pressure under different bedding angles. Overall, as confining pressure increases, the brittleness of Longmaxi Formation shale gradually weakens, which is consistent with the change of brittleness with confining pressure concluded by AE characteristics. However, under different bedding angles, $BI_4 \sim BI_8$ also experience obvious fluctuations and even show reverse brittleness changes over the increase of confining pressure. Such fluctuation states and reverse brittleness variations are also found in research by Yang et al. (2020) and Rahimzadeh Kivi et al. (2018). For example, at bedding angles of 0° and 45° , BI_5 , BI_6 , and BI_7 fluctuate with the increase of confining pressure, respectively; at bedding angles of 30° and 45° , BI_4 and BI_8 even show an increasing trend with the increase of confining pressure (after 50 MPa confining pressure), which cannot reasonably reflect the influence of confining pressure on brittleness. Although $BI_4 \sim BI_8$ can show that the overall brittleness of shale decreases with the rise of confining pressure, it experiences fluctuations, which is not conducive to accurately evaluating the brittleness of Longmaxi Formation shale. The major reason is that BI_4 only considers the influence of pre-peak elastic strain on the brittleness of

shale, while brittleness is defined by BI_5 , BI_6 , BI_7 , and BI_8 only according to the form of the post-peak stress–strain curve, which causes $BI_4 \sim BI_8$ to fluctuate and experience reverse brittleness with the change of confining pressure. Figure 33 shows the variation trend of normalized BI with bedding angle under different confining pressures. $BI_4 \sim BI_8$ change obviously with the bedding angle, indicating the brittleness of Longmaxi Formation shale also changes with bedding angle. Notably, according to the AE characteristics of Longmaxi Formation shale analyzed previously, the brittleness will show a variation trend of “first decrease and then increase” with the increase of bedding angle. However, it can be seen from Fig. 33 that even under the same confining pressure, the changes of $BI_4 \sim BI_8$ with bedding angle are not consistent. This phenomenon once again shows that $BI_4 \sim BI_8$ defined only by considering the form of the stress–strain curve before and after the peak does not seem to fully reflect the brittleness variation of Longmaxi formation shale. The brittleness index should be defined in combination with the characteristics of stress–strain curve before and after the peak of the Longmaxi formation shale.

Figure 34 describes the stress–strain curves with the same peak stress σ_f and residual stress σ_r (C_1 , C_2 , C_3 , C_4 , C_5 , C_6). It can be seen from Fig. 34 that the pre-peak and post-peak characteristics of stress–strain curves with the same peak stress and residual stress are inconsistent, which represents the different degrees of brittleness. For example, although the pre-peak characteristics of C_4 , C_5 , and C_6 curves are consistent, the decrease rate of stress with strain is not the same after the peak, and the rock shows different brittleness degrees, which cannot be accurately described by BI_7 . Meanwhile, although the magnitude of post-peak strength loss is the same for C_2 and C_5 (C_3 and C_6), the pre-peak plastic strain accumulation rates are different, and BI_8 cannot accurately describe the change of brittleness. Therefore, based on BI_7 and BI_8 , this study considers the characteristics

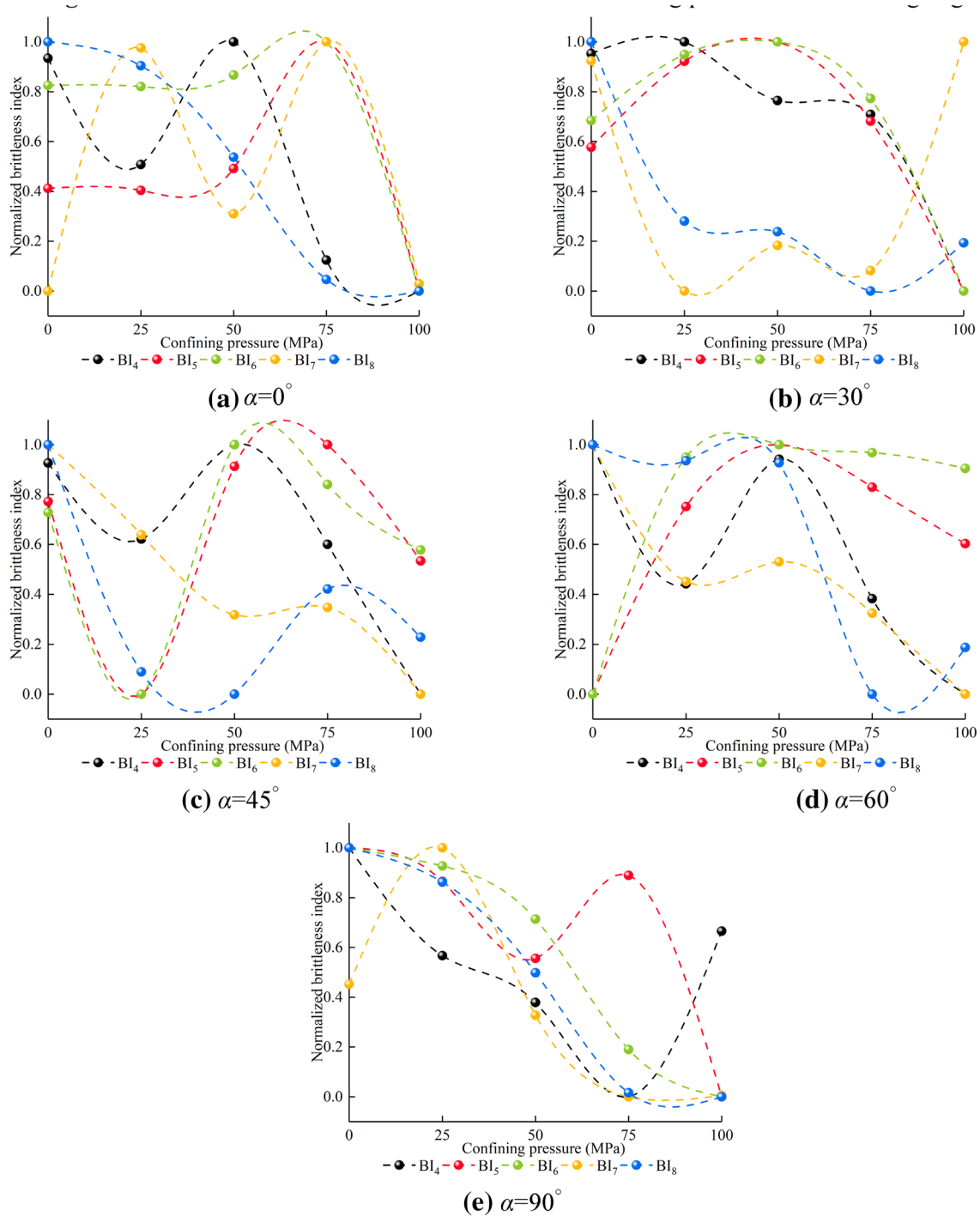


Fig. 32 Normalized brittleness index under different confining pressures

of the stress–strain curve before and after the peak of the Longmaxi formation shale and proposes a new brittleness index BI_{new}, as shown in the following:

$$BI_{new} = \frac{\sigma_f \cdot \lg N}{\sigma_f - \sigma_{cd}} BI_8. \tag{18}$$

By further simplifying Eq. (18)

$$BI_{new} = \frac{\sigma_f - \sigma_r}{\sigma_f - \sigma_{cd}} \lg |M| \cdot \lg N, \tag{19}$$

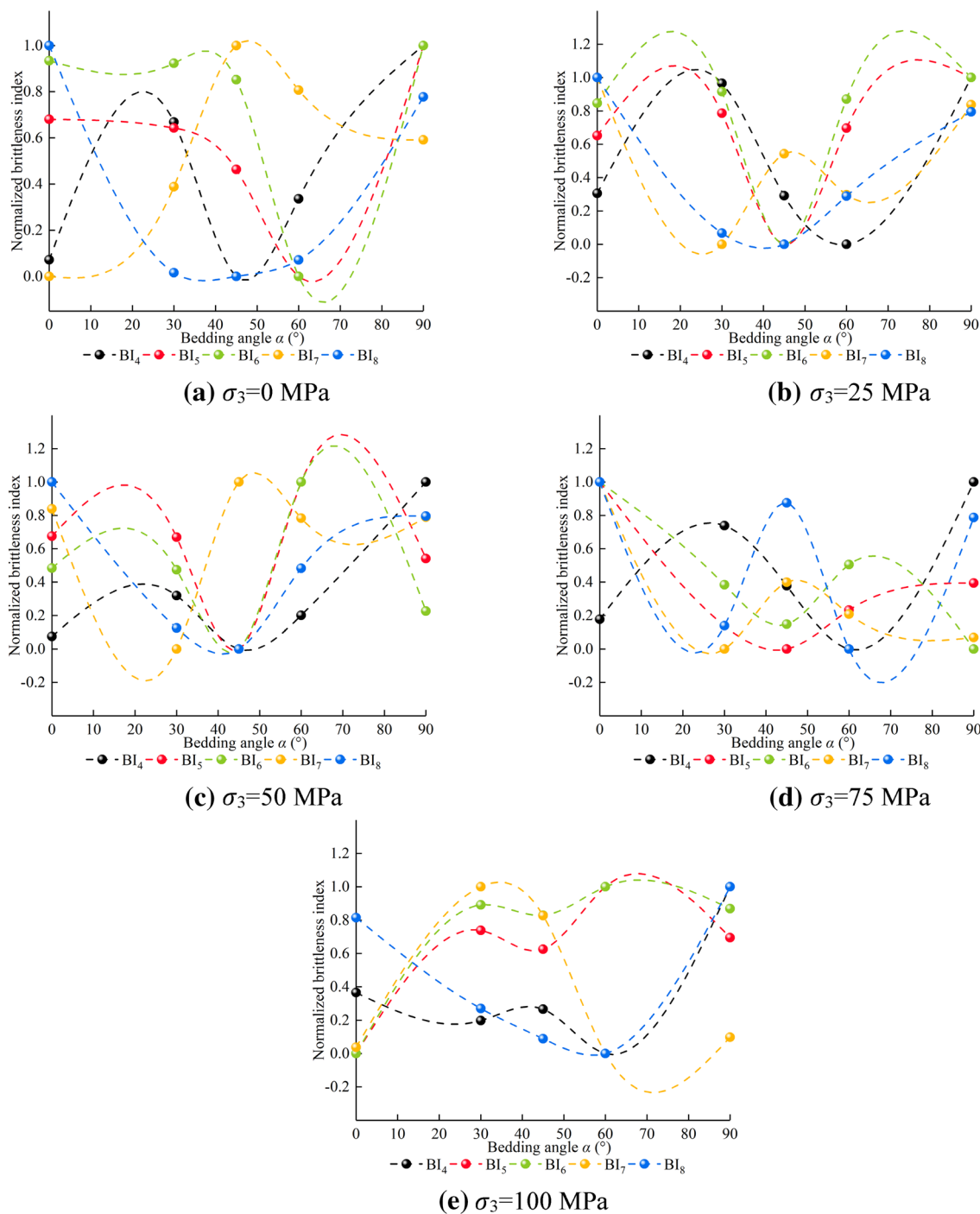


Fig. 33 Normalized brittleness index under different bedding angles

where N represents the slope of the secant between the cracks damage stress σ_{cd} and peak stress σ_f . The larger value of N means the brittleness characteristic before the peak of the stress–strain curve is more obvious, as shown in Fig. 34.

The changes of BI_{new} and normalized BI_{new} with confining pressure and bedding angle are obtained in combination with Eq. (19), as described in Figs. 35 and 36, respectively.

BI_{new} gradually decreases with the rise of confining pressure, and shows a changing pattern of “first decrease and then increase” with the increase of bedding angle, which is consistent with the analysis of the brittleness of Longmaxi Formation shale by AE characteristics. It shows that BI_{new} can better reflect the change of brittleness of Longmaxi formation shale with confining pressure and bedding angle.

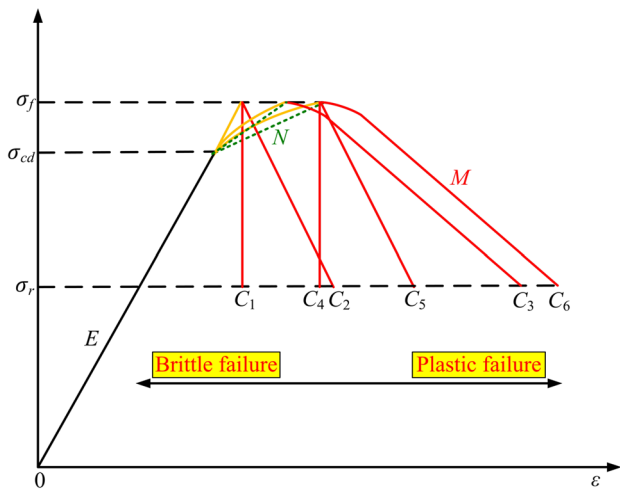
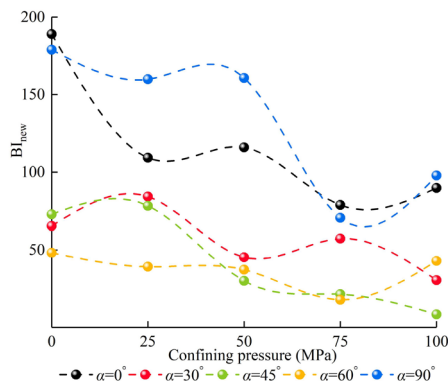


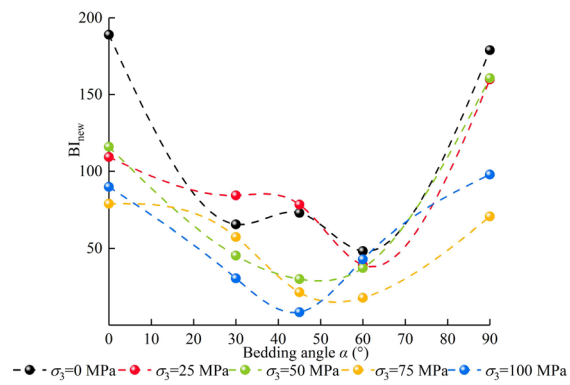
Fig. 34 Stress–strain curves with the same peak stress and residual strength but showing different degrees of brittleness

Therefore, it can be found that there is a correlation between brittleness and failure modes in view of the changes

in brittleness and failure modes of Longmaxi Formation shale with confining pressure and bedding angle. Under low confining pressure, due to the weak binding effect of confining pressure, the elastic energy is released violently when the shale sample is damaged; the shale sample mainly experiences tensile splitting failure, and the shale is brittle. As confining pressure increases, the binding effect of confining pressure becomes stronger, and the shale sample undergoes shear failure. At this time, the shale will slide along the fracture surface, causing further plastic deformation and energy dissipation and the brittleness of shale is reduced. According to the variation of brittleness and failure modes with confining pressure, the brittleness of shale samples in Co-Sh, Sp-Al or Sp-Th failure modes is significantly higher than that of Sh-Al or Sh-Th failure modes. Furthermore, because the matrix of shale is stronger than the bedding plane, once the bedding plane is damaged, cracks will grow rapidly along the bedding plane, resulting in a violent release of elastic energy and a sharp reduction in stress. Compared with the fracture through the bedding plane, the failure along the bedding plane is easier, and the shale samples damaged along

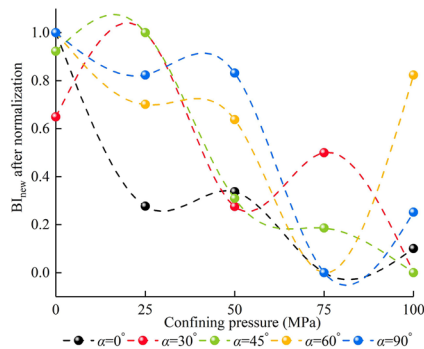


(a) Variation of BI_{new} with confining pressure.

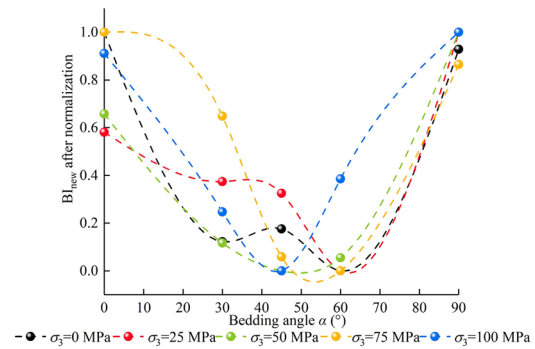


(b) Variation of BI_{new} with bedding angle.

Fig. 35 Variation of BI_{new} with confining pressure and bedding angle



(a) Variation of normalized BI_{new} with confining pressure.



(b) Variation of normalized BI_{new} with bedding angle.

Fig. 36 Variation of BI_{new} after normalization with confining pressure and bedding angle

the bedding plane show stronger brittleness. Thus, the brittleness of shale samples in the Sp-Al failure mode is higher than that of the Sp-Th failure mode, and the brittleness of the Sh-Al failure mode is also higher than that of the Sh-Th failure mode. In essence, the Co-Sh failure mode refers to the combination of shear cracks passing through the bedding plane and shear failure along the bedding plane under low confining pressure. Based on the above analysis, the brittleness of the Co-Sh failure mode should be less than the Sp-Th failure mode. Therefore, the brittleness degree represented by five failure modes can be expressed as Sp-Al > Sp-Th > Co-Sh > Sh-Al > Sh-Th.

In conclusion, the brittleness of Longmaxi Formation shale is tightly related to the AE response characteristics and failure modes. AE response characteristics can not only qualitatively characterize the brittleness level of shale, but also visually represent the failure process and modes of Longmaxi Formation shale. The final failure modes can reflect the brittleness level, and the brittleness also determines the change of shale failure modes.

5 Conclusions

In this paper, conventional uniaxial/triaxial compression tests were carried out on the Longmaxi formation shale from Changning, Sichuan Basin, China. The mechanical properties, AE characteristics, and failure modes of shale under different confining pressures and bedding angles were studied, and the effects of anisotropy on deformation, strength and failure characteristics of shale were analyzed. Meanwhile, AE technology and a variety of brittleness indexes (including the new index BI_{new} proposed in this study) were used to evaluate the brittleness of the Longmaxi formation shale under different confining pressure and bedding angles. Finally, the relationship between AE characteristics, brittleness, and failure modes of shale was also discussed. The main conclusions are as follows:

1. There is no significant microcracks compaction stage in the stress–strain curve of Longmaxi Formation shale, which mainly experiences the near-linear elastic deformation stage I, bedding activation and stable microcracks' propagation stage II, bedding initiation slip and unstable microcracks propagation stage III, and bedding severely slips and post-peak failure stage IV. Increasing confining pressure helps to improve the compressive strength of shale and reduce the anisotropy. Shale has significant anisotropy under high confining pressure, and it must be considered when shale gas is exploited in deep shale. Otherwise, there will be large errors in fracturing geometric parameter design and fracturing effect prediction.

2. The mechanical properties of Longmaxi Formation shale can be described by the Mohr–Coulomb criterion, Hoek–Brown criterion, Nova criterion, Jaeger criterion, and Saeidi criterion. Results show that the Saeidi criterion and Nova criterion can better reflect the test results than the Mohr–Coulomb criterion and Hoek–Brown criterion. The five strength criteria are all able to describe the effect of confining pressure on compressive strength and anisotropy, and the unique performance that the “dangerous bedding angle” will change in the process of confining pressure increasing.
3. AE monitoring results show that AE evolution can qualitatively characterize the brittleness of shale. The denser the distribution of AE events, the smaller the peak value of AE ringing count, the smoother the rise of cumulative ring counts and cumulative energy with time, and the lower the brittleness of Longmaxi formation shale; when the trigger rate of AE events is lower and the peak value of the AE ringing count of a single event is higher, cumulative ring counts and cumulative energy will change suddenly in stage IV and increase sharply with time, and the brittleness is higher. During the progressive failure process of shale, the distribution of peak frequency is different in various stages, which is also significantly affected by confining pressure and bedding angle.
4. The failure modes of Longmaxi Formation shale are equipped with significant confining pressure effect and bedding effect. The failure modes can be divided into five types: conjugate shear failure (Co-Sh), splitting through bedding plane (Sp-Th), shear along bedding plane (Sh-Al), and shear through bedding plane (Sh-Th). The brittleness index BI_{new} proposed in this paper is consistent with the brittleness results of shale analyzed by AE evolution, which can better describe the variation of brittleness with confining pressure and bedding angle. The AE response characteristics of Longmaxi formation shale can not only qualitatively characterize the brittleness of shale but also show the failure process and modes of shale samples. Meanwhile, the different brittleness determines the change of failure modes, and the failure modes also reflect the brittleness of shale. The brittleness represented by the five failure modes can be expressed as Sp-Al > Sp-Th > Co-Sh > Sh-Al > Sh-Th.

Acknowledgements This research was funded by the National Natural Science Foundation of China (Grant Nos. U20A20266, 51874202), Major Talent Projects (2020), China, and Special Plan Young Top-notch Talent of China.

Declarations

Conflict of Interest The authors declare that they have no known conflicts of interest or personal relationships that could have appeared to influence the work reported in this paper.

Data availability statement The test data used to support the findings of this study are included within the article. Readers can obtain data supporting the research results from the test data table in the paper.

References

- Altindag R (2002) The evaluation of rock brittleness concept on rotary blast hole drills. *J South Afr Inst Min Metall* 102(1):61–66
- Amann F, Kaiser P, Button EA (2012) Experimental study of brittle behavior of clay shale in rapid triaxial compression. *Rock Mech Rock Eng* 45(1):21–33
- Arora S, Mishra B (2015) Investigation of the failure mode of shale rocks in biaxial and triaxial compression tests. *Int J Rock Mech Min Sci* 79:109–123
- Ashour HA (1988) A Compressive Strength Criterion for Anisotropic Rock Materials. *Can Geotech J* 25(2):233–237
- Barnhoorn A, Primarini M and Houben M (2016) Fracturing and brittleness index analyses of shales. EGU 2016:EPSC2016-5869
- Benson PM et al (2010) Laboratory simulation of volcano seismicity. *Science* 322(5899):249–252
- Bi C, Wang Y, Xie W, Sun W, Liu W (2020) Prestack AVO inversion for brittleness index of shale based on BI_Zoeppritz equation and NSGA II. *Acta Geophys* 68(2):1082
- Bishop A (1967) Progressive failure—with special reference to the mechanism causing it. In: *Proceeding of Geotech. Conf., Oslo*, pp 142–150
- Brown E (1997) Practical estimates of rock mass strength. *Int J Rock Mech Min Sci*
- Byerlee J (1978) A review of rock mechanics studies in the United States pertinent to earthquake prediction. *Pure Appl Geophys* 116(4):586–602
- Cai W, Zhu H, Liang W (2022) Three-dimensional tunnel face extrusion and reinforcement effects of underground excavations in deep rock masses. *Int J Rock Mech Min Sci* 150:104999
- Chandler M, Meredith P, Crawford B (2013) Experimental determination of the fracture toughness and brittleness of the Mancos shale, Utah. *Br J Psychiatry* 184(6):110–117
- Chen Y, Jin Y, Chen M, Yi Z, Zheng X (2017) Quantitative evaluation of rock brittleness based on the energy dissipation principle, an application to type II mode crack. *J Nat Gas Sci Eng* 45:527–536
- Cheng W, Jin Y, Chen M (2015) Reactivation mechanism of natural fractures by hydraulic fracturing in naturally fractured shale reservoirs. *J Nat Gas Sci Eng* 27:1357–1365
- Cho J-W, Kim H, Jeon S, Min K-B (2012) Deformation and strength anisotropy of Asan gneiss, Boryeong shale, and Yeoncheon schist. *Int J Rock Mech Min Sci* 50:158–169
- De S, Perić D and Owen D (1950) *The mathematical theory of plasticity*. Oxford University Press.
- Duveau G, Shao JF, Henry JP (1998) Assessment of some failure criteria for strongly anisotropic geomaterials. *John Wiley & Sons Ltd* 3(1):1–26
- Fairhurst CE, Hudson JA (1999) Draft ISRM suggested method for the complete stress-strain curve for intact rock in uniaxial compression. *Int J Rock Mech Min Sci Geomech Abstracts* 36(3):281–289
- Geng Z et al (2016) Experimental study of brittleness anisotropy of shale in triaxial compression. *J Nat Gas Sci Eng* 36:510–518
- Guan X, Yi X and Yang H (2014) Contrast of shale gas reservoir conditions in China and the United States. *J Southwest Petrol Univ (Science & Technology Edition)* 36(5):33–39
- Guo W, Shen W, Li X, Wang N, Zhou S (2020) Study on mechanical characteristics and damage mechanism of the Longmaxi Formation shale in southern Sichuan Basin. *China Energy Explor Exploit* 38(2):454–472
- Hajiabdolmajid V, Kaiser P (2003) Brittleness of rock and stability assessment in hard rock tunneling. *Tunn Undergr Space Technol* 18(1):35–48
- Hajiabdolmajid VR (2001) Mobilization of strength in brittle failure of rock. Queen's University at Kingston (Canada)
- Hatheway AW (2009) The complete ISRM suggested methods for rock characterization, testing and monitoring; 1974–2006. *Environ Eng Geosci* 15(1):47–48
- Heng S, Guo Y, Yang C, Daemen JJK, Li Z (2015) Experimental and theoretical study of the anisotropic properties of shale. *Int J Rock Mech Min Sci* 74:58–68
- Hiroki S, Mark D, Zoback (2013) Mechanical properties of shale-gas reservoir rocks — Part 1: Static and dynamic elastic properties and anisotropy. *Geophysics* 78(5):D381–D392
- Hoek E (1980) *Underground excavations in rock*. London: Institution of Mining and Metallurgy.
- Hucka V, Das B (1974a) Brittleness determination of rocks by different methods. *Int J Rock Mech Min Sci Geomech Abstracts* 11(10):389–392
- Hucka V, Das B (1974b) Brittleness determination of rocks by different methods. *Int J Rock Mech Min Sci Geomech Abstracts* 11(10):389–392
- Huo Z et al (2018) An improved evaluation method for the brittleness index of shale and its application—a case study from the southern north China basin. *J Nat Gas Ence Eng* 59:47–55
- Jaeger J (1960a) Shear failure of transversely isotropic rock. *Geol Mag* 97:65–72
- Jaeger JC (1960b) Shear failure of anisotropic rocks. *Geol Mag* 97(01):65
- Jarvie D, Hill R, Ruble T, Pollastro R (2007) Unconventional shale-gas systems: the Mississippian Barnett Shale of north-central Texas as one model for thermogenic shale-gas assessment. *AAPG Bull* 91:475–499
- Jin X, Shah SN, Roegiers JC, Zhang B (2015) An integrated petrophysics and geomechanics approach for fracability evaluation in shale reservoirs. *SPE J* 20(03):518–526
- Kuila U, Dewhurst DN, Siggins AF, Raven MD (2011) Stress anisotropy and velocity anisotropy in low porosity shale. *Tectonophysics* 503(1–2):34–44
- Labuz JF, Zang A (2012) *Mohr-coulomb failure criterion*. Springer International Publishing
- Lawal L and Mahmoud M (2020) Poisson's ratio, porosity and aspect ratio as geomechanical index of shale brittleness. *International Petroleum Technology Conference*
- Lee YK, Pietruszczak S (2008) Application of critical plane approach to the prediction of strength anisotropy in transversely isotropic rock masses. *Int J Rock Mech Min Sci* 45(4):513–523
- Lee WJ, Sohn SY (2014) Patent analysis to identify shale gas development in China and the United States. *Energy Policy* 74(nov.):111–115
- Li X et al (2016a) Breakdown pressure and fracture surface morphology of hydraulic fracturing in shale with H₂O, CO₂ and N₂. *Geomech Geophys Geo-Energy Geo-Resour* 2(2):63–76
- Li Y, Li Y, Wang B, Chen Z, Nie D (2016b) The status quo review and suggested policies for shale gas development in China. *Renew Sustain Energy Rev* 59:420–428
- Li H, Zhong Z, Liu X, Sheng Y, Yang D (2018) Micro-damage evolution and macro-mechanical property degradation of limestone due to chemical effects. *Int J Rock Mech Min Sci* 110:257–265

- Li N et al (2018) Acoustic emission response of laboratory hydraulic fracturing in layered shale. *Rock Mech Rock Eng* 51(11):3395–3406
- Li C, Gao C, Xie H, Li N (2020) Experimental investigation of anisotropic fatigue characteristics of shale under uniaxial cyclic loading. *Int J Rock Mech Min Sci* 130:104314
- Lin B, Li Z (2020) Analysis of the natural gas demand and subsidy in China: a multi-sectoral perspective. *Energy* 202:117786
- Lin L, Zhang J, Tang X, Jing T, Zhu L (2013) Conditions of continental shale gas accumulation in China. *Natural Gas Industry*
- Lin C, He J, Li X, Wan X, Zheng B (2017) An experimental investigation into the effects of the anisotropy of shale on hydraulic fracture propagation. *Rock Mech Rock Eng* 50(3):543–554
- Liu Q, Liang B, Sun W, Zhao H, Ghorbel E (2021) Experimental study on the difference of shale mechanical properties. *Adv Civ Eng* 2021:1–14
- Lockner D (1993) The role of acoustic emission in the study of rock fracture. *Int J Rock Mech Min Sci Geomech Abstracts* 30(7):883–899
- Lyu C, Liu J, Ren Y, Liang C, Liao Y (2021a) Study on very long-term creep tests and nonlinear creep-damage constitutive model of salt rock. *Int J Rock Mech Min Sci* 146:104873
- Lyu C et al (2021b) Experimental study on mechanical properties, permeability and acoustic emission characteristics of gypsum rock under THM coupling. *Rock Mech Rock Eng* 54(11):5761–5779
- Lyu C, Liu J, Ren Y, Liang C, Zeng Y (2022) Mechanical characteristics and permeability evolution of salt rock under thermal-hydro-mechanical (THM) coupling condition. *Eng Geol* 302:106633
- Ma X et al (2017) Hydraulic fracture propagation geometry and acoustic emission interpretation: a case study of Silurian Longmaxi Formation shale in Sichuan Basin. *SW China Petrol Explor Dev* 44(6):1030–1037
- Martin CD (1996) Brittle failure of rock materials: test results and constitutive models. *Can Geotech J* 33(2):378–378
- Martin HR, Erling F, Olavmagnar N, Tayseer AH (2011) A shaly look at brittleness. *American Rock Mechanics Association*
- Mclamore RT and Gray KE (1967) A strength criterion for anisotropic rocks based upon experimental observations. *Soc Petrol Eng*
- Niandou H, Shao JF, Henry JP, Fourmaintraux D (1997) Laboratory investigation of the mechanical behaviour of Tournemire shale. *Int J Rock Mech Min Sci* 34(1):3–16
- Nishiyama T et al (2002) The examination of fracturing process subjected to triaxial compression test in Inada granite. *Eng Geol* 66(3):257–269
- Nova R (1980) The failure of transversely isotropic rocks in triaxial compression. *Int J Rock Mech Min Sci Geomech Abstracts* 17(6):325–332
- Ohnaka M, Mogi K (1982) Frequency characteristics of acoustic emission in rocks under uniaxial compression and its relation to the fracturing process to failure. *J Geophys Res* 87(B5):3873–3884
- Pietruszczak S, Mroz Z (2001) On failure criteria for anisotropic cohesive-frictional materials. *Int J Numer Anal Meth Geomech* 25(5):509–524
- Qi M, Giraud A, Colliat JB, Shao JF (2016) A numerical damage model for initially anisotropic materials. *Int J Solids Struct* 100–101:245–256
- Rafiai H (2011) New empirical polyaxial criterion for rock strength. *Int J Rock Mech Min Sci* 48(6):922–931
- Rahimzadeh Kivi I, Ameri M, Molladavoodi H (2018) Shale brittleness evaluation based on energy balance analysis of stress-strain curves. *J Petrol Sci Eng* 167:1–19
- Ramamurthy T (1993) Strength and modulus responses of anisotropic rocks. *Comprehensive rock engineering* 1: 313–329
- Rao KS, Rao GV, Ramamurthy T (1986) A strength criterion for anisotropic rocks. *Indian Geotech J* 16(4):317–333
- Ren Y, Yang Z, Lu M, Yan X and Li X (2018) A new rock brittleness index based on energy dissipation in the process of uniaxial or triaxial compression test. In: 80th EAGE Conference and Exhibition 2018
- Ren W, Lau HC (2020) Analytical modeling and probabilistic evaluation of gas production from a hydraulically fractured shale reservoir using a quad-linear flow model. *J Petrol Sci Eng* 184:106516
- Rickman R, Mullen MJ, Petre JE, Grieser WV and Kundert D (2008) A practical use of shale petrophysics for stimulation design optimization: all shale plays are not clones of the barnett shale, SPE Annual Technical Conference and Exhibition: 115258
- Rune et al (2015) Brittleness of shales: relevance to borehole collapse and hydraulic fracturing. *J Petrol Sci Eng* 131: 200–209
- Runar N, Gutierrez M, Bratli RK, Høeg K (2006) Brittle–ductile transition, shear failure and leakage in shales and mudrocks. *Mar Petrol Geol* 23(2):201–212
- Rybacki E, Reinicke A, Meier T, Makasi M, Dresen G (2015) What controls the mechanical properties of shale rocks?—Part I: strength and Young’s modulus. *J Petrol Sci Eng* 135:702–722
- Rybacki E, Meier T, Dresen G (2016) What controls the mechanical properties of shale rocks?—Part II: brittleness. *J Petrol Sci Eng* 144:39–58
- Saeidi O, Vaneghi RG, Rasouli V, Gholami R (2013) A modified empirical criterion for strength of transversely anisotropic rocks with metamorphic origin. *Bull Eng Geol Env* 72(2):257–269
- Shao et al (2015) Numerical simulation of damage and failure in brittle rocks using a modified rigid block spring method. *Comput Geotech* 64: 48–60
- Shi X, Yang X, Meng Y, Li G (2016) An anisotropic strength model for layered rocks considering planes of weakness. *Rock Mech Rock Eng* 49(9):1–10
- Singh M, Samadhiya NK, Kumar A, Kumar V, Singh B (2015) A nonlinear criterion for triaxial strength of inherently anisotropic rocks. *Rock Mech Rock Eng* 48(4):1387–1405
- Tan P et al (2017) Analysis of hydraulic fracture initiation and vertical propagation behavior in laminated shale formation. *Fuel* 206:482–493
- Tarasov B, Potvin Y (2013) Universal criteria for rock brittleness estimation under triaxial compression. *Int J Rock Mech Min Sci* 59:57–69
- Tien YM, Kuo MC, Juang CH (2006) An experimental investigation of the failure mechanism of simulated transversely isotropic rocks. *Int J Rock Mech Min Sci* 43(8):1163–1181
- Tsai SW, Wu EM (1971) A general theory of strength for anisotropic materials. *J Compos Mater* 5(1):58–80
- Wang J et al (2018) A study on the mechanical behavior and statistical damage constitutive model of sandstone. *Arab J Sci Eng* 43(10):5179–5192
- Wang S, Zhong Z, Liu X (2020) Development of an anisotropic nonlinear strength criterion for geomaterials based on SMP criterion. *Int J Geomech* 20(3):04019183.1-04019183.12
- Weber CL, Clavin C (2012) Life cycle carbon footprint of shale gas: review of evidence and implications. *Environ Sci Technol* 46(11):5688–5695
- Wei J, Duan H and Yan Q (2021) Shale gas: Will it become a new type of clean energy in China? — A perspective of development potential. *J Clean Prod* 294: 1024–1031
- Weleman H, Goidescu C, Pensée V and Kondo D (2016) A micro-mechanical damage model for initially anisotropic materials. *Int J Rock Mech Min Sci* 77: 122–132
- Wilson GM (2013) *Underground excavations in rock*: Hoek, E; Brown, E T London: Institution of Mining and Metallurgy, 1980, 527P. *International Journal of Rock Mechanics and Mining Sciences & Geomechanics Abstracts* 18(2):27

- Wu S, Ge H, Wang X, Meng F (2017) Shale failure processes and spatial distribution of fractures obtained by AE monitoring. *J Nat Gas Sci Eng* 41:82–92
- Yagiz S (2009) Assessment of brittleness using rock strength and density with punch penetration test. *Tunn Undergr Space Technol* 24(1):66–74
- Yang Y, Sone H, Hows A and Zoback MD (2013) Comparison of brittleness indices in organic-rich shale formations. *IEICE Trans Electron* 25: 871–881
- Yang S-Q, Yin P-F, Huang Y-H (2019) Experiment and discrete element modelling on strength, deformation and failure behaviour of shale under brazilian compression. *Rock Mech Rock Eng* 52(11):4339–4359
- Yang S-Q, Yin P-F, Ranjith PG (2020) Experimental study on mechanical behavior and brittleness characteristics of longmaxi formation shale in changning, sichuan basin. *China Rock Mech Rock Eng* 53(5):2461–2483
- Yang K, Yan Q, Zhang C, Wu W and Wan F (2021) Study on mechanical properties and damage evolution of carbonaceous shale under triaxial compression with acoustic emission. *Int J Damage Mech* 5(1):105678952199119
- Yao C et al (2016) A discrete approach for modeling damage and failure in anisotropic cohesive brittle materials. *Eng Fracture Mech* 155:102–118
- Yi et al (2016) Experimental study of brittleness anisotropy of shale in triaxial compression. *J Nat Gas Sci Eng* 36: 510–518
- Yong MT, Ming CK (2001) A failure criterion for transversely isotropic rocks. *Int J Rock Mech Min Sci* 38(3):399–412
- Yuan H, Wu K, Chen Z, Kai Z and Perdomo M (2015a) New models of brittleness index for shale gas reservoirs: weights of brittle minerals and rock mechanics parameters. *Asia Pacific Unconventional Resources Conference & Exhibition*
- Yuan J, Luo D, Feng L (2015b) A review of the technical and economic evaluation techniques for shale gas development. *Appl Energy* 148(jun. 15):49–65
- Zhai M, Wang Z, Zhang L, Li A and Li L (2021a) Investigation on the anisotropy of mechanical properties and brittleness characteristics of deep laminated sandstones. *Eng Geol* 251: 128–145
- Zhang D, Ranjith PG, Perera MSA (2016) The brittleness indices used in rock mechanics and their application in shale hydraulic fracturing: a review. *J Petrol Sci Eng* 143:158–170
- Zhang J et al (2018) Energy-based brittleness index and acoustic emission characteristics of anisotropic coal under triaxial stress condition. *Rock Mech Rock Eng* 51(11):3343–3360
- Zhang F, Damjanac B, Maxwell S (2019a) Investigating hydraulic fracturing complexity in naturally fractured rock masses using fully coupled multiscale numerical modeling. *Rock Mech Rock Eng* 52(12):5137–5160
- Zhang Q et al (2019b) Experimental investigation on permeability evolution of limestone caprock under coupled THM processes. *KSCE J Civ Eng* 23(12):5090–5097
- Zhao X, Kang J, Bei L (2013) Focus on the development of shale gas in China—Based on SWOT analysis. *Renew Sustain Energy Rev* 21(may):603–613
- Zhao C et al (2022) Experimental study on mechanical properties, permeability and energy characteristics of limestone from through-coal seam (TCS) tunnel. *Eng Geol* 303:106673
- Zhou HW, Wang ZH, Ren WG, Liu ZL, Liu JF (2019) Acoustic emission based mechanical behaviors of Beishan granite under conventional triaxial compression and hydro-mechanical coupling tests. *Int J Rock Mech Min Sci* 123:104125
- Zou C, Cheng Y, Li J (2021) Strain rate and size effects on the brittleness indexes of Carrara marble. *Int J Rock Mech Min Sci* 146:104860
- Zou C, Yingying S, Liu K, Cheng Y, Li J (2022) Feasibility of artificial materials in simulating rock failure based on rate-dependent brittleness indexes. *Rock Mech Rock Eng* 55:4999–5027
- Zurich et al (2007) Seismicity preceding volcanic eruptions: new experimental insight. *Geology* 35(2): 183–186

Publisher's Note Springer Nature remains neutral with regard to jurisdictional claims in published maps and institutional affiliations.

Springer Nature or its licensor (e.g. a society or other partner) holds exclusive rights to this article under a publishing agreement with the author(s) or other rightsholder(s); author self-archiving of the accepted manuscript version of this article is solely governed by the terms of such publishing agreement and applicable law.